Astron. Astrophys. 322, 878–895 (1997)

ASTRONOMY
AND
ASTROPHYSICS

A possible origin for X-rays from O stars

A. Feldmeier, J. Puls, and A.W.A. Pauldrach

Universitäts-Sternwarte, Scheinerstr. 1, D-81679 München, Germany

Received 10 October 1996 / Accepted 16 November 1996

Abstract. X-ray spectra of hot, massive stars provide convincing evidence for thermal emission that extends far out into their stellar winds. Accordingly, strong shocks were proposed as sources of the X-ray emission, where the shocks result from the line-driven instability. We show from hydrodynamic simulations that the emission from individual shocks which grow out of initially small perturbations may fall one or two orders of magnitude below the observed flux. Instead, we find that mutual collisions of dense shells of gas formed in deep wind regions can lead to shocks with a much stronger emission which almost matches the observed flux.

This model predicts strong variability of the X-ray emission, which is not observed. We propose that – in contrast to the presently assumed spherical symmetry of the wind – the emission stems from a large number of independent, radial cones so that fluctuations average out over the whole emitting volume.

Key words: stars: early-type – X-rays: stars – hydrodynamics – instabilities – shock waves

1. Introduction

Over the past years, it has become possible to determine fundamental stellar parameters like radii and masses from quantitative spectroscopy of radiation driven winds of hot, luminous stars (Kudritzki & Hummer 1990; Pauldrach et al. 1994; and references therein). The recently proposed wind-momentum luminosity relation (Kudritzki et al. 1995) opens the prospect of using OBA supergiants as extragalactic distance indicators. A vexing problem, however, which affects the detailed analyses of the winds, is their non-stationarity. Observational evidence for this comes especially from (i) the so-called discrete absorption components, which propagate through the absorption troughs of unsaturated P Cygni profiles (Prinja & Howarth 1986; Henrichs 1988; Prinja & Fullerton 1994); and (ii) the strong X-ray fluxes from essentially all OB stars, which are nowadays interpreted to be indicative of vigorous flow disruptions. The X-ray emission, e.g., may have severe implications for the ionization balance in the wind (Pauldrach et al. 1994; MacFarlane et al. 1994). In the present paper we investigate certain wind features which result from the strong line-driven instability, and which may be the origin of the X-ray emission.

Send offprint requests to: A. Feldmeier. feld@usm.uni-muenchen.de

1.1. Observations

a) X-ray luminosity. The most distinctive property of the X-ray emission from O stars is the scaling of their X-ray luminosity with the bolometric luminosity, $L_x/L_{\rm bol} \approx 10^{-7}$ (Harnden et al. 1979; Seward et al. 1979; Long & White 1980; Pallavicini et al. 1981; Cassinelli et al. 1981). Sciortino et al. (1990) find from the EINSTEIN catalog of 289 Galactic O stars that $L_x \propto L_{\rm bol}^{\alpha}$, with $\alpha = 1.08$ $(-0.22, +0.06)$, and a mean value $\log(L_x/L_{\rm bol}) = -6.4$. However, the total range of values reaches from -5.4 to -7.4 (Chlebowski et al. 1989). From detailed spectral fits to ROSAT PSPC data for 42 O stars, Kudritzki et al. (1996) find $\log(L_x/L_{\rm bol}) = -6.7$ with somewhat tighter bounds of -6.0 and -7.2. The range of validity of the $L_x/L_{\rm bol}$ relation seems to be confined to the O stars: from ROSAT observations of near-main-sequence B stars, Cassinelli et al. (1994) find that $\log(L_x/L_{\rm bol}) \approx -7$ holds only up to spectral type B1. By B3, the X-ray luminosity has already dropped to $10^{-9} L_{\rm bol}$. Furthermore, Wessolowski (1996) finds *no* relationship between L_x and $L_{\rm bol}$ from ROSAT PSPC data for 61 WN-type Wolf-Rayet stars. With the availability of large stellar samples and/or high-quality spectral data it has recently become possible to search for weaker dependence of L_x on other stellar parameters than $L_{\rm bol}$: Sciortino et al. (1990) from the EINSTEIN catalog find no correlation of L_x with the wind terminal velocity, stellar rotation rate, and mass loss rate; but they do find strong correlations with the wind momentum flux, $\dot{M} v_\infty$ ($\dot{M}$ the mass loss rate; v_∞ the terminal velocity), and with the wind kinetic energy flux, $\frac{1}{2}\dot{M} v_\infty^2$. In contrast, Kudritzki et al. (1996) find a strong correlation of the temperature of X-ray emitting gas (which was not considered by Sciortino et al. 1990) with the ratio $\frac{1}{2}\dot{M} v_\infty^2 / L_{\rm bol}$, and a strong correlation of L_x with $\dot{M}/v_\infty$, where the latter quantity is an (approximate) measure of the mean wind density. However, more systematic studies are still needed.

b) Spectrum. The X-ray spectra of OB stars are consistent with a thermal origin in a plasma of temperatures 10^6 to a few

10^7 K. To achieve good *fits* to the data using a thermal emission model, three prerequisites have been found to be necessary over the years (Cassinelli et al. 1981; Cassinelli & Swank 1983; Hillier et al. 1993; Corcoran et al. 1993, 1994; Cohen et al. 1996; Feldmeier et al. 1996): (i) wind absorption has to be included, especially for soft X-rays below 1 keV; (ii) the X-ray emission must extend far out into the wind; and (iii) a temperature stratification has to be assumed (or at least two independent hot components). *Direct* observational evidence for the thermal origin of the X-ray emission comes from the recent detection of line emission using the BBXRT and ASCA (Corcoran et al. 1993, 1994). (However, already Cassinelli & Swank 1983 found emission near 2 keV in the EINSTEIN SSS spectrum of ζ Ori, which they suggested could be *interpreted* as line emission.) Waldron (1991) finds direct evidence for wind absorption from a correlation between X-ray hardness ratio and 6 cm radio data. Finally, we mention that the derived filling factors of hot gas are on the order of 0.1 to 1% for O stars (Hillier et al. 1993) and may possibly approach unity for near-main-sequence B stars (Cassinelli et al. 1994).

c) Variability. Collura et al. (1989) analyzed EINSTEIN IPC data of 12 OB stars for variability. Three stars were found to be long-term variables above the 4σ significance level, e.g., ζ Puppis with an effective fractional amplitude of $\approx 40\%$ in the soft band on a time scale of $\gtrsim 1$ day. Only τ Sco was found to show marginal short-time variability (above the 3σ significance level) during a time scale of ≈ 50 s and with fractional amplitude 30%. However, as reported in Berghöfer & Schmitt (1994a), a reanalysis of the data by the above authors provided no evidence for variability of ζ Pup. Cassinelli et al. (1994) did not find variability on time scales larger than 1 ks for any of the 12 near-main-sequence B stars they surveyed with the ROSAT PSPC. The short-time variability below 1 ks that was found for 3 stars – e.g. for τ Sco with period of 125 s – was attributed to spacecraft wobble. The study of Berghöfer & Schmitt (1994a) using ROSAT PSPC data gives no indication of variability for σ Ori and ζ Ori (the latter star will be the principal subject of the present paper) on time scales from hour(s) to 3 years – with the one notable exception (Berghöfer & Schmitt 1994b) of a 30% increase in the count rate of ζ Ori in the hard band (0.6 to 2.4 keV) from Sept 23 to Sept 25, 1992. The count rate then returned to its value before the increase over the next ≈ 0.5 to 1 year. In contrast, during Sept 19/20, 1991 the level of absolute variations in the X-ray count rate of this star was well below 10% for 20 observations taken with an average integration time of ≈ 1000 s. The analysis of 57 OB stars from the ROSAT all-sky survey also showed no significant variability on a time scale of ≈ 2 days (Berghöfer & Schmitt 1995). A recent, interesting detection of X-ray variability is reported in Berghöfer et al. (1996) for ζ Pup: they find a *periodic* modulation with $P = 16.7$ hours both in the equivalent width of the Hα line and in the count rate between 0.9 and 2.0 keV, the latter with an amplitude of 6%. This modulation is indicative of periodic variations in the density at the wind base.

1.2. Critical review of previous models

We review here the mechanisms proposed for the X-ray emission from single O stars. This rules out colliding winds as sites of X-ray emission. We also do not consider shocks close to wind compressed disks – the latter proposed by Bjorkman & Cassinelli (1993) to occur possibly for Be stars.

a) Base corona. Hearn (1972, 1973) suggested the dissipation of radiation driven sound waves as a mechanism of chromospheric or coronal heating in hot stars, and estimated the thickness of a base corona (Hearn 1975) from the equivalent width of Hα to be $\approx 1\ R_*$ for ζ Ori. The latter number was revised downwards to be smaller than $0.1\ R_*$ by Cassinelli et al. (1978). Cassinelli & Olson (1979) studied a coronal model to explain the observed superionization in OB star winds by Auger ionization. However, soon after the launch of the EINSTEIN satellite, this base corona model was found to be inconsistent with the X-ray data from O stars (Long & White 1980; Cassinelli et al. 1981; Cassinelli & Swank 1983), since the soft X-rays below 1 keV were not so strongly attenuated by wind absorption as the slab model would suggest. Especially, the K-shell edge of oxygen at ≈ 0.6 keV was not detected. A corona as dominant X-ray source was also ruled out for the O4 If star ζ Puppis from the non-detection of the coronal [Fe XIV] 5303 Å line (Baade & Lucy 1987). – Waldron (1984) proposed a recombination stellar wind model for early-type stars where the wind is thermally initiated by a corona, and at some distance from the star the gas cools and recombines to make radiative driving efficient. Due to the large emission measure of the corona, helium is mostly doubly ionized, thereby reducing the wind opacity for X-rays. Still, this model is subject to the same principal criticisms as the static corona and can also be ruled out (Cassinelli & Swank 1983; Baade & Lucy 1987).

b) Blob model. Lucy & White (1980) proposed a phenomenological model for the structure of unstable line-driven winds (where the instability mechanism was suggested by Lucy & Solomon 1970). Here, radiatively driven clumps plough through ambient wind gas, where the latter is shadowed by the blobs and is therefore not radiatively driven; X-rays should then originate from the shocks preceding the blobs. While free parameters of the model can be adjusted to give the observed X-ray luminosity of, e.g., ζ Pup, the spectrum is inconsistent with the observations: since the bow shocks should have maximum strength close to the star, soft X-ray attenuation is again far too strong in this model (Lucy 1982; Cassinelli & Swank 1983).

c) Forward shocks. The blob model was revised by Lucy (1982) to include the effect of blob-blob shadowing. The gas dynamical description was modified from a sequence of blobs to a sawtooth-like sequence of radiatively driven forward shocks. Here, inner shocks shadow outer shocks and cause them to decay. As a consequence of this shock destruction mechanism, X-ray emission can continue far out into the terminal flow. Although, for the first time, a strong flux of soft X-rays is predicted in accordance with the observations, the model suffers from the shortcoming (Lucy 1982; Cassinelli & Swank 1983) that the predicted X-ray luminosity is a factor of ≈ 20 too small. How-

ever, by the ad hoc assumption that a small number of shocks is exceptionally strong, the model can be brought into agreement with the data (Cassinelli & Swank 1983).

d) Inverse Compton scattering. (This model only attempts to explain an eventual extra component of hard X-ray emission.) White (1985) identified the nonthermal radio emission from some of the most luminous hot stars (Abbott et al. 1984; Bieging et al. 1989) with synchrotron radiation from electrons which are accelerated to relativistic speeds by the first-order Fermi mechanism in wind shocks of the type proposed by Lucy (1982). Pollock (1987) and Chen & White (1991) proposed that inverse Compton scattering of stellar UV photons by this relativistic electrons can generate hard X-ray emission at energies larger than 2 keV (and γ-ray emission up to 50 MeV). (However, due to this Compton cooling these relativistic electrons close to the star cannot survive to large radii to produce the above mentioned synchrotron radiation: therefore, as proposed by White & Chen 1992 and Chen & White 1994, the accelerating shocks have to propagate beyond the radio photosphere at > 100 stellar radii to supply fresh relativistic electrons.) The emerging spectra should follow a power law, $F_\nu \propto E^{-1/2}$, which could explain the shallow decline of the SSS data for three Orion belt stars (Cassinelli & Swank 1983): the measured decline is indeed much flatter than the exponential tail of a thermal component with temperature of a few million degrees as derived from the spectrum below 2 keV.

e) Reverse shocks. After the fundamental finding of Owocki et al. (1988) that the line-driven instability of early-star winds leads to the formation of strong *reverse* shocks instead of strong forward shocks, MacFarlane & Cassinelli (1989) set up a phenomenological model for the thin wind of τ Scorpii (B0 V). Here, a large base perturbation leads to the formation of a double shock – a pair of strong reverse and forward shocks enclosing a dense shell – which propagates out through the wind. By adjusting the strength of the shock (via the base perturbation), this double shock can reproduce the EINSTEIN spectra of τ Sco within an order of magnitude. – First results on X-ray synthesis from full hydrodynamic simulations, where hot gas evolves from the growth of initially small perturbations due to the line-driven instability, are due to Cooper & Owocki (1992, 1994) and Cooper (1994; cf. also Cohen et al. 1996). They use a different approach for the thin winds of early B stars near the main sequence, and for thick winds of O supergiants: for thin winds, radiative cooling is assumed to be unimportant, and only adiabatic cooling is included in the energy equation. This leads to large amounts of hot gas in the wind – however, still not enough to explain the observed X-ray luminosity. This is another hint that in thin winds large fractions of the gas must be X-ray emitting (Cassinelli et al. 1994). For thick winds, on the other hand, Cooper & Owocki (1992) report severe numerical problems with including radiative cooling. They therefore calculate an *isothermal* wind structure, which should be a fairly good approximation to the actual wind dynamics because of short radiative cooling zones. From the properties of the calculated shocks (their mass inflow and velocity jump, i.e., their temperature), Cooper & Owocki calculate the corresponding X-ray spectra by assuming *steady-state* radiative cooling zones of known emission behind these shocks. Surprisingly, the calculated X-ray luminosity for their O supergiant model is a factor of 10 *larger* than the observed value (while the spectral shape is about the same). We shall return to this issue in Sect. 3.

In the following we present an extension to this last item, e). We find in our models that single reverse shocks give an X-ray emission which is typically one or two orders of magnitude below the observed flux. Yet, mutual collisions of dense shells of gas compressed in the shocks give rise to a much stronger emission which can almost reproduce the observations. The paper is organized as follows. After a discussion of our technique of hydrodynamic simulations and X-ray synthesis in Sect. 2, we examine in Sect. 3 the X-ray emission from the wind structure at selected instants. This will give the clue to the origin of strong emission in shell-shell collisions, which are the topic of Sect. 4. The dichotomy between the observed constancy of X-ray emission and the variability of synthesised spectra is discussed in Sect. 5. Finally, Sect. 6 gives a summary and prospects for future work.

2. Technique

2.1. Hydrodynamics

The continuity, radial momentum, and energy equation for a spherically symmetric flow (the latter approximation is discussed below) are,

$$\frac{\partial \rho}{\partial t} + \frac{1}{r^2}\frac{\partial}{\partial r}\left(r^2 \rho v\right) = 0 \tag{1}$$

$$\frac{\partial (\rho v)}{\partial t} + \frac{1}{r^2}\frac{\partial}{\partial r}\left(r^2 \rho v^2\right) = -\frac{\partial p}{\partial r} - \rho g + \rho g_l, \tag{2}$$

$$\frac{\partial e}{\partial t} + \frac{1}{r^2}\frac{\partial}{\partial r}\left(r^2 e v\right) = -\frac{p}{r^2}\frac{\partial}{\partial r}\left(r^2 v\right) - Q(\rho, T), \tag{3}$$

where the standard symbols are used, and where g_l is the radiative line acceleration; e is the thermal energy density, which for an ideal gas is $e = p/(\gamma - 1)$; in the following, $\gamma = 5/3$ is assumed. Q is the total power radiated per unit volume. (We neglect heating by re-absorption.)

The assumptions underlying our present approach are the same as in Feldmeier (1995), with the formulation of the line force as developed by Owocki et al. (1988) and Owocki (1991). We here only discuss some central concepts.

(1) We use a standard time-explicit, Eulerian finite difference scheme (cf. Reile & Gehren 1991) to solve the above equations on staggered grids. The advections terms are calculated using van Leer (1977) fluxes through the boundaries of adjacent control volumes, and we apply the so-called "consistent advection" after Norman et al. (1980). At the inner boundary – which is chosen to be the stellar photosphere of continuum optical depth unity – we use the method of Thompson (1987, 1990) to fix the Riemann invariants, here in an exponential density stratification through which a perturbation propagates. At the highly supersonic outer boundary, zeroth order extrapolation is

adequate. – For details on the operator splitting sequence, artificial viscosity to smear out shock fronts, and the calculation of pressure work and radiative cooling (including time step limitations), see Feldmeier (1995). We add here that heat conduction is not included in our present simulations. While heat conduction may be important at temperatures $\gtrsim 10^7$ K (e.g., MacFarlane & Cassinelli 1989), we accept the error introduced by neglecting it in favor of keeping the number of physical processes and interacting phenomena small.

(2) Spherical symmetry is a severe restriction of the present approach, and is only justified by computational demands. While in the final section of this paper we shall interpret the calculated hydrodynamical structures as corresponding approximately to independent radial wind cones of small opening angle, our procedure for X-ray synthesis (cf. below) assumes full 4π symmetry – so that fluctuations in the hydrodynamical structure lead to strong X-ray variability, cf. Sect. 5.

(3) The line force is calculated by using the so-called "smooth source function" method (Owocki 1991; Owocki & Puls 1996). The total force is the sum – weighted by the line-strength distribution function of Castor et al. (1975) – of the force on a singlet transition, for which a pure Doppler profile and a constant mass absorption coefficient κ is assumed. The latter should be a good approximation for strong resonance lines and lines with a lower metastable level, both of which dominate the line force. We assume further that no line-overlap occurs. The force on a single line is calculated via a formal integral with prespecified, local source function. In the present paper we use a source function which corresponds to purely geometric dilution of the radiation field, i.e., to optically thin lines. To calculate the flux, the Doppler width of a line is resolved by three frequency points, where the frequency integral extends over ± 3 Doppler widths. The angle integral is approximated by a one-ray quadrature, and, finally, the temperature dependence of the line force is taken into account using the results of MacGregor et al. (1979)

(4) In the expression for the total power radiated, $Q = n_{\rm e} n_{\rm H} \Lambda(T)$, we use a power law fit to the Raymond et al. (1976) cooling function for an optically thin plasma, $\Lambda(T) = A\,(T/T_0)^{\delta}$, with $\delta = -1/2$, $T_0 = 10^6$ K, and $A = 1.6 \times 10^{-22}$ erg cm^3 s^{-1}. While an interval-wise power-law fit would be more accurate, we use the above global approximation in order to keep the temporal evolution of the cooling layer due to the oscillatory thermal instability (Langer et al. 1981, 1982) as simple as possible – since, as discussed by Walder & Folini (1996), this evolution shows a complex dependence on the value of δ. The significance of this oscillation for stellar wind simulations is that the cooling zone of minimum extent during each cycle is shorter than any achievable grid resolution. This results in a "loss" of the cooling layer, i.e., the shock collapses to an *isothermal* shock. To prevent this, we alter the cooling function to have a *stable* exponent $\delta = 2$ below some temperature $T_{\rm swi}$ (Feldmeier 1995). We use here $T_{\rm swi} = 15\,T_{\rm eff}$ (= 4.7×10^5 K; see below): smaller $T_{\rm swi}$ can essentially not prevent the collapse of cooling zones, while larger $T_{\rm swi}$ would influence the soft X-ray spectrum emitted.

In the present paper we study an O supergiant wind model with stellar parameters (listed in Table 1) close to that of ζ Ori. This star should be an ideal candidate to test X-ray emission models since: (i) it has among the highest signal-to-noise ratio within our full sample of 42 O stars observed with the ROSAT PSPC (Kudritzki et al. 1996); and (ii) its stellar and wind parameters are known to a good accuracy. Additionally, there are no indications that helium recombines in the wind of ζ Ori. In contrast, for the dense wind of the O supergiant ζ Puppis, Hillier et al. (1993) found evidence that helium recombines to He^+ from about 6 R_* on. This enhances the background opacity enormously, and consequently these authors concluded that the observed X-rays at ≈ 0.5 keV must be emitted from radii larger than 30 R_*, and X-rays below 0.2 keV from $r > 100$ R_*. With our present hydrodynamic models we see no possibility to generate or maintain the corresponding amounts of hot gas at these large distances (cf. Sect. 3). However, since ζ Pup is possibly the only, at most one of a very few stars in our sample which shows helium recombination, we feel justified to analyse the X-ray emission properties of the more standard candidate ζ Ori instead, and leave the re/investigation of the peculiar wind of ζ Pup (especially the location of He recombination) to a future study.

Photospheric parameters for ζ Ori are taken from Voels et al. (1989), while the wind terminal velocity and interstellar hydrogen column density are from Haser (1995). For the mass loss rate we assume an average of the results obtained by Lamers & Leitherer (1993) from Hα, $\dot{M} = 3.9 \times 10^{-6}$ M$_\odot$/yr, the reanalysis of these data by Puls et al. (1996), $\dot{M} = 3.6 \times 10^{-6}$ M$_\odot$/yr for $\beta = 1$, and the value from radio measurements, again from Lamers & Leitherer (1993), $\dot{M} = 2.5 \times 10^{-6}$ M$_\odot$/yr. As a typical value for O star winds, we set the CAK exponent to $\alpha = 0.7$ (cf. Pauldrach et al. 1986), and the line force constant is fixed at a value which results in the average above mass loss rate, $\dot{M} = 3 \times 10^{-6}$ M$_\odot$/yr. The line strength cutoff $\kappa_{\rm m}$ of Owocki et al. (1988) terminates the line list at the strongest lines, in order to prevent the development of subgrid structure. The thermal speed is representative for driving ions like C, N, and O. Finally, the photospheric barometric scale height and the acoustic cutoff period (above which sound waves cannot propagate vertically through the atmosphere) are listed in Table 1.

2.2. Photospheric perturbation

In time-dependent wind simulations so far (Owocki et al. 1988; Owocki 1992), a photospheric sound wave is assumed to trigger perturbations that grow in the presence of the line-driven instability. However, the coherence of the wave leads to a periodic wind structure, at least for small wave amplitudes. As will become clearer in later sections, the amount of hot gas in this regular structure is too small to explain the observed X-ray flux. Therefore, to generate more hot gas in the wind, we propose two different types of irregular perturbations which should lead to enhanced dynamical interactions in the wind, e.g. shell collisions, and therefore possibly to enhanced heating.

Table 1. Stellar parameters for ζ Ori.

Spectral type		O9.7 Ib
Temperature	$T_{\rm eff}$	31 500 K
Mass	M	$34\,M_\odot$
Gravity	$\log g$	3.2
Radius	R_*	$24\,R_\odot$
Luminosity	L	$5.1\times10^5 L_\odot$
Terminal speed	v_∞	1 850 km/s
Mass loss rate	$\dot{M}$	$3\times10^{-6}\,M_\odot$/yr
Helium fraction	$n_{\rm He}/n_{\rm H}$	0.1
Distance	d	450 pc
ISM column density	$\log(N_{\rm H}\,{\rm cm}^2)$	20.34
Thomson coefficient	σ_e	$0.34\,{\rm cm}^2/{\rm g}$
Eddington factor	Γ	0.39
CAK exponent	α	0.7
Line force constant	$\kappa_0\,v_{\rm th}/c$	$5950\,{\rm cm}^2/{\rm g}$
Line strength cutoff	$\kappa_{\rm m}/\kappa_0$	10^{-3}
Sound speed (isoth.)	a	20.7 km/s
Thermal speed	$v_{\rm th}$	$0.3\,a$
Scale height	H	$2.6\times10^{-3}\,R_*$
Acoustic cutoff period	$T_{\rm cut}$	7.34 h

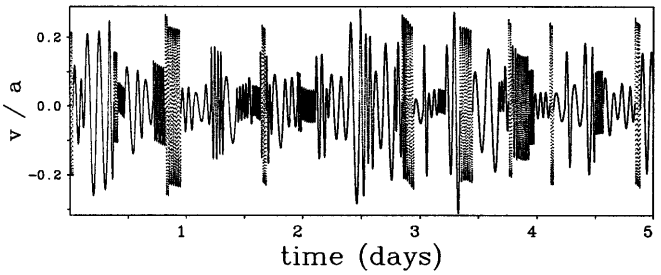

Fig. 1. Time series of the radial photospheric velocity (in units of the isothermal sound speed) due to a "tunable" sound wave.

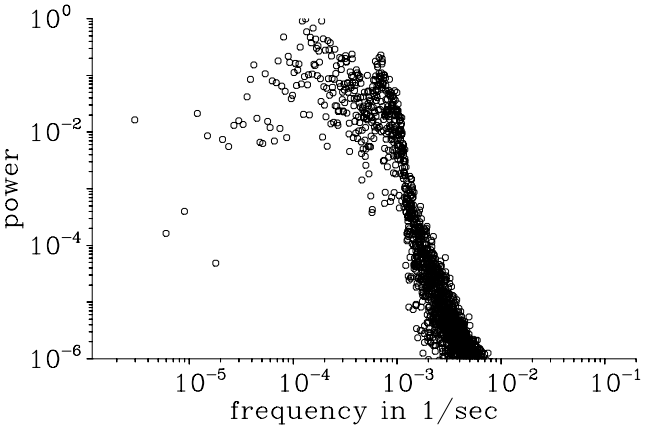

Fig. 2. Power spectrum of the sound wave from Fig. 1.

The first is a kind of "tunable" sound wave, where at certain instants the amplitude and period of the wave changes abruptly. More specifically, after a certain coherence time T has elapsed, over which the wave has an amplitude A and period P, we choose three random numbers $0 < \xi_T, \xi_A, \xi_P < 1$ to define a new coherence time, wave amplitude, and wave period by

$$X = X_{\rm m}^{(1-\xi_X)}\, X_{\rm M}^{\xi_X}\,. \tag{4}$$

Here, X stands for any of T, A, or P, and subscripts 'm' or 'M' refer respectively to the prespecified minimum or maximum of the corresponding quantity. To avoid discontinuities in the amplitude, we furthermore apply these changes only after a full wave cycle is finished. Finally, $T_{\rm m} = P_{\rm m} = 10^3$ s and $T_{\rm M} = P_{\rm M} = 10^4$ s is chosen, and we consider the two cases $A_{\rm M} = 0.3$ resp. 0.5, where $A_{\rm M}/A_{\rm m} = 10$ is assumed. The time series of the photospheric velocity for $A_{\rm M} = 0.3$ is shown in Fig. 1, its power spectrum in Fig. 2.

While our perturbation amplitudes are chosen to be as large as possible (to generate strong wind structure) – yet still be subsonic in the photosphere (see below) – the perturbation *periods* are determined from the following considerations. The radiative force which acts on the extremely rarefied, optically thin gas between strong wind shocks (for a discussion of the typical wind structure see Sect. 3) causes unresolvably steep velocity fields. This led Owocki et al. (1988) to introduce the cutoff parameter $\kappa_{\rm m}$, by which much shallower, numerically manageable velocity gradients are achieved. To still be able to reach shock velocity jumps which are large enough to heat gas to X-ray temperatures, Owocki et al. (1988) induced large *distances* between subsequent wind shocks by applying photospheric perturbations with long wavelengths, i.e., with periods as those above. However, one has to keep in mind that maximally unstable (harmonic) perturbations have a much shorter wavelength (typically by a factor of 100) which is on order of the Sobolev length and below (Owocki & Rybicki 1984; where the stationary wind speed grows by an ion thermal speed over a Sobolev length). Therefore, it seems possible that – opposite to the wind models to be discussed in the following – strong structure may (more naturally?) also develop on much shorter lengthscales. However, such structure is not easily anticipated, and clarification has to come from future numerical simulations.

To ensure that waves with periods as short as 1000 seconds (actually even 500 s) can propagate on the numerical grid, we use 250 equidistant grid points from 1 R_* to 1.05 R_*. At the latter radius the wind is already highly supersonic (6.5 a), and the Doppler effect has stretched the wavelength so that a coarser grid is appropriate. Over the next 3750 points, a logarithmic grid with ${\rm d}r/r = const$ is laid out to 30 R_*. Finally, a short grid with 20 points establishes a smooth link of differentials ${\rm d}r$ between the above two grids.

As a second type of photospheric perturbation we consider the physically somewhat more meaningful Ornstein-Uhlenbeck (1930) stochastic process (where the latter are generalizations of discrete Markovian chains to a continuous time variable). This process is set up here for the stochastic variable u (the velocity perturbation), and mimics photospheric turbulence via a solu-

tion of the Langevin equation (cf. Wax 1954 for a collection of classical papers on the subject, and Risken 1989 for a textbook),

$$\frac{\mathrm{d}u}{\mathrm{d}t} + \frac{u}{t_\mathrm{c}} = \Gamma(t), \tag{5}$$

where t_c is the relaxation time. The fluctuating or stochastic force, $\Gamma(t)$, has zero mean (ensemble averages understood) and a correlation function which corresponds to white noise (the meaning of the constant q becomes clearer from the next equation),

$$\begin{aligned} \langle \Gamma(t) \rangle &= 0, \\ \langle \Gamma(t_1)\Gamma(t_2) \rangle &= q\delta(t_1 - t_2). \end{aligned} \tag{6}$$

The velocity correlation function is then, for times $t_1, t_2 \gg t_\mathrm{c}$ found to be (cf. Risken 1989, p. 34),

$$\langle u(t_1)u(t_2) \rangle = \tfrac{1}{2} q t_\mathrm{c}\, e^{-|t_1 - t_2|/t_\mathrm{c}}, \tag{7}$$

which gives for time intervals $|t_1 - t_2| \ll t_\mathrm{c}$,

$$D(\tau) \equiv \langle (u(t+\tau) - u(t))^2 \rangle \propto \tau, \tag{8}$$

where D is the so-called structure function. The relation $D \propto \tau$ is also found for the *Lagrangian* structure function for fluid turbulence in the Kolmogorov inertial range (cf. Landau & Lifshitz 1989, p. 132; Monin & Yaglom 1987, Sects. 21.2 to 21.4). The use of the Langevin equation to describe Lagrangian fluid turbulence is reviewed by Pope (1994); cf. also Gail et al. (1974). – In contrast, however, the inertial range structure function in the *Eulerian* frame is found to be $D(\tau) \propto \tau^{2/3}$ (Landau & Lifshitz), so that our use of the Langevin equation to generate a stochastic process with spectrum $E \propto \omega^{-2}$ (white noise) at a fixed *location* – i.e., the photosphere – can only be a very approximate description for inertial range turbulence, which has a spectrum $E \propto \omega^{-5/3}$ instead.

For the two models presented in Sect. 3 we have chosen (via the above variable q) a velocity dispersion $\sigma_u/a = 0.1$ and 0.25. Due to the Gaussian distribution of $u(t)$, this corresponds roughly to $A_\mathrm{M} = 0.2$ and 0.5, cf. Fig. 3. As relaxation time we assume, in accordance with the periods from the foregoing sound wave model, $t_\mathrm{c} = 5000$ s. The time series of the Langevin process is shown in Fig. 3, and its power spectrum in Fig. 4. Notice the white noise form of the spectrum, $E(\omega) \sim \omega^{-2}$, for frequencies larger than ${t_\mathrm{c}}^{-1}$.

Finally, we turn to a brief discussion of the physical significance of these photospheric perturbations. Using Fourier techniques to separate turbulent ("Gaussian") from rotational velocity fields in observed helium profiles, Conti & Ebbets (1977) and Ebbets (1979) find a turbulent velocity dispersion of ≈ 30 km/s, i.e. $\approx 1.5\, a$ for hot supergiants. Even with the principal criticism that it is not quite clear as to which degree these analyses apply to *expanding* atmospheres (Mihalas 1979 and references therein; Kudritzki 1992; Haser 1995), our turbulent photospheric velocity fields of maximum amplitude $\delta v/a = 0.2 \ldots 0.5$ used in the present paper should lie within the margins allowed by observations.

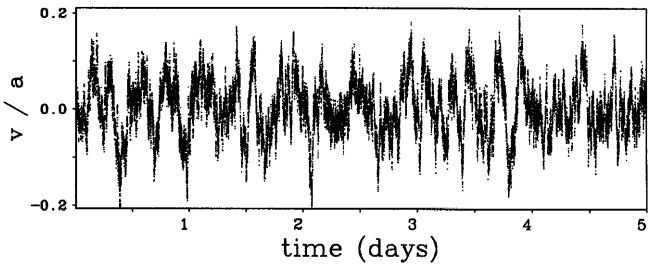

Fig. 3. Time series of the photospheric velocity due to Langevin turbulence.

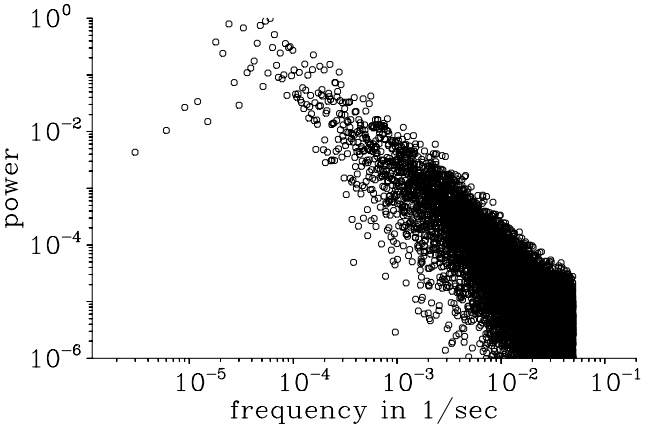

Fig. 4. Power spectrum of the signal in Fig. 3.

At least two other types of photospheric perturbations which may trigger structure formation in the wind are discussed in the literature: pulsations (for non-radial pulsations in general: Baade 1991; Fullerton et al. 1996; Gies 1996); for strange mode pulsations: Gautschy & Glatzel 1990; Glatzel 1994) and macroscopic magnetic fields (with emphasis on dipoles: Underhill & Fahey 1984; Stahl et al. 1993; Bohlender 1994; Henrichs et al. 1994). However, since the azimuthal coherence scales of both pulsations and macroscopic magnetic fields are large, they should be connected (if there is such a connection at all) with "large-scale" phenomena in the wind, especially with the so-called discrete absorption components (Cranmer & Owocki 1996) and/or the so-called "bananas" (Owocki et al. 1995) observed in non-saturated P Cygni profiles. – In contrast, the observed constancy of the X-ray fluxes from OB stars gives strong evidence for the stochastic nature of the emission process. We return to this issue in Sect. 5.

2.3. Synthesis of X-ray spectra

To calculate the X-ray spectrum emitted from a structured, spherically symmetric wind we use a formal integral approach (cf. Hillier et al. 1993; Feldmeier et al. 1996). The absorption coefficient is given as the sum of bound-free and line opacities for the cold wind taken from a stationary NLTE model for ζ Ori, and the K-shell opacity for the elements C, N, O, Ne, Mg, Si, S (Daltabuit & Cox 1972). The X-ray emission of hot gas is

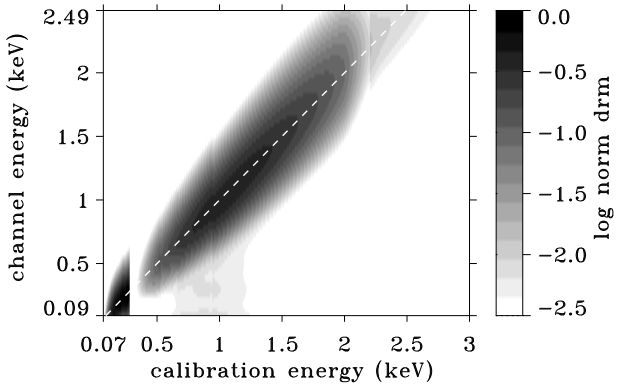

Fig. 5. Greyscale rendition of the ROSAT detector response matrix (drm; including effective detector area) appropriate for observations of ζ Ori. The dashed white line indicates a detector with infinite resolution. The null-response at 0.28 keV is due to the Carbon edge of the entrance window material.

calculated using the recent version of the Raymond & Smith (1977) code. Finally, ISM opacities are calculated after Morrison & MacCammon (1983), and the ROSAT detector response matrix used to convert incident photon fluxes to count rates is shown in Fig. 5.

The spectrum shown in Fig. 8 (identical to the one in Feldmeier et al. 1996) consists of 53 single observations taken over 1.5 years, with integration times typically from 500 to 1500 seconds. The *episodic* event from Sept 23 to 25 in 1992, when the count rate increased by $\approx$ 30% (Berghöfer & Schmitt 1994b) is *not* included in our data set, which reaches only to Sept 19, 1992. The dashed line in the figure is a best *fit* to the data using the empirical X-ray emission model of Hillier et al. (1993) where isothermal hot regions of radius-independent temperature and filling factor are assumed to be distributed through the whole wind. This fit serves here to find the approximate spectrum incident on the detector (before being convolved with the drm), which is shown as dashed line in the lower panel of Fig. 8. The corresponding "stellar" emergent spectrum gives an X-ray luminosity in the ROSAT energy band of $L_x = 4.9 \times 10^{32}$ erg/s.

3. The X-ray emission at selected instants

In this section we discuss the X-ray emission from the wind at certain instants when the calculated and observed spectra agree well. This serves mainly to identify the hot gas responsible for the emission and to discuss its properties, which suggests that this gas originates in radial shell-shell collisions. These are the topic of the next section.

3.1. A wind model out to 100 R_*

As a preparatory consideration we have to determine the spatial extent of the wind relevant for X-ray emission. To this end we ran a simulation out to 100 R_*. This model uses 7000 grid points, with 1000 points spaced equidistantly up to 1.1 R_*, and 6000 points spaced according to $\mathrm{d}r/r = const$ out to 100 R_*; the tunable sound wave was used as the triggering perturbation. The simulation took somewhat more than one cpu month on a $\approx$ 20 Mflop workstation, until a model time of 10 days. At this time, the gas initially located at the inner boundary had reached the outer boundary, and the whole computational domain was influenced by (previous) photospheric perturbations which triggered the formation of wind structure, and possibly of hot regions.

Fig. 6 shows a snapshot of the density, velocity, and temperature of the wind at t = 10 d. The dashed line corresponds to a stationary wind with a β = 0.8 velocity law (Pauldrach et al. 1986), which serves as an initial condition. The structure caused by unstable growth at radii below 10 R_* has been described by Owocki et al. (1988) and Owocki (1991, 1992) so that we limit ourselves here to some additional remarks, especially on the outer wind structure. – Primary radiative reverse shocks are destroyed around 5 R_* (Feldmeier 1995). A strong shock which is seen in the velocity field of Fig. 6 at $\approx$ 5.5 R_* is a forward shock (preshock side at large radii, postshock side at small radii), and can be termed a "secondary" shock in that it is not directly caused by the radiative instability, but is due to fast, cold, inner gas ramming into slow, hot, outer gas. This latter, very rarefied intershell gas – which is spread over almost 2 R_*! – was at former times heated in a reverse shock which was meanwhile destroyed. Since all driving ions are stripped, the radiative force on this hot gas is negligible and the gas stalls. Furthermore, because of its low density, radiative cooling is very inefficient, and the gas can only cool via adiabatic expansion on its advection to outer wind regions. No essentially new ingredients to the wind dynamics occur in the outer regions $> 20 \ldots 30$ R_*. Occasionally (e.g., at $\approx$ 65 R_* in Fig. 6), relatively strong forward shocks similar to the one just described form at the inner edge of an old, hot region. We furthermore find a few, rather strong reverse shocks in the outer wind, e.g., at 20 and 24 R_* in Fig. 6. They show the same characteristics as inner reverse shocks, i.e., very rarefied gas is accelerated to high velocities by the large radiative force on optically thin lines, until this fast gas undergoes a decelerating shock transition. However, we never find more than three or four of these shocks over the full range from 10 to 100 R_*. The gross appearence of the outer structure is that of a return to a smooth wind: remaining hot gas cools, velocity gradients smooth out, and the dense shells expand, which leads to a homogenization of the mass distribution. Since typical velocity differences inside the shell are of the order of the sound speed, both the inertia and pressure forces are of the same magnitude and the shell expansion is due to their combined action.

We mention here as a side remark that one has to be cautious about estimating the extent of cooling zones behind wind shocks from *stationary* wind conditions. Such estimates may differ significantly from the cooling lengths found in dynamical simulations, especially since in the latter case the gas in front of reverse shocks is extremely rarefied, and since furthermore a hierarchy of mutual shock collisions causes abrupt changes in the cooling zones.

We find that for the above model, at all times, the total spatial domain from 30 to 100 R_* contributes *less than a few permille* to

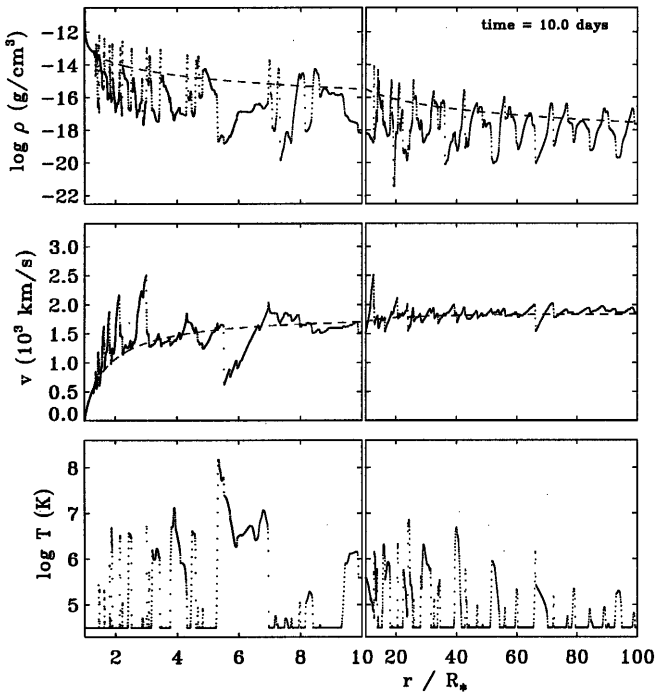

Fig. 6. Snapshot out to 100 stellar radii of the wind perturbed by a tunable photospheric sound wave. The density, velocity, and temperature are marked at each numerical grid point. The dashed line corresponds to a stationary wind with β = 0.8 velocity law.

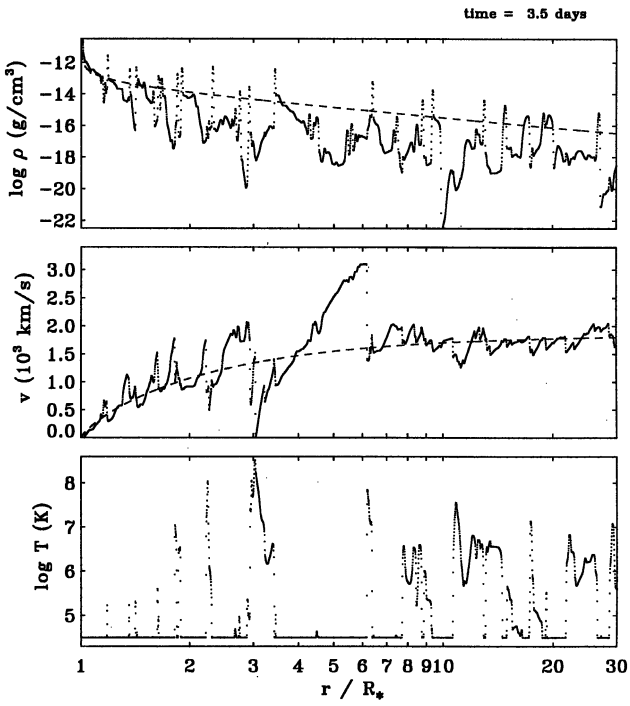

Fig. 7. Snapshot of the wind structure 3.5 d after model start. The photospheric disturbance is a tunable sound wave.

the total X-ray emission from the structured wind. This justifies our consideration of only the restricted range from 1 to 30 R_* in the following models. (The wind attenuation of X-rays from 30 R_* to infinity is calculated assuming a stationary wind with $v = v_\infty$ and $\rho \propto r^{-2}$.)

3.2. Photospheric sound wave as wind perturbation

Fig. 7 shows a snapshot of the wind perturbed by the tunable photospheric sound wave of maximum amplitude $A_{\rm M}$ = 0.5, at 3.5 days after model start. A strong *forward* shock occurs slightly above 3 R_*, and terminates only at *negative* gas velocities. (In the vicinity of this forward shock, at $r \lesssim 3\ R_*$, a strong reverse shock is found.) Such negative velocities appear regularly in the present models with large perturbation at the wind base. However, this gas is extremely rarefied and does not contribute in any observable manner to the X-ray emission; consequently we forgo here a discussion of the reality of this inflow. The second, very pronounced shock in Fig. 7 is located slightly above 6 R_*. The significance of this reverse shock will be seen below.

Farther out from this very strong shock (with a velocity jump of 1700 km/s!), only a few more, much weaker reverse shocks occur (at $\approx 8, 10, 21, 28\ R_*$), which heat gas to soft X-ray temperatures of $\approx 1 \times 10^6$ K. Yet, the bulk of the outer hot gas is just leftover from former shock destruction.

The top panel of Fig. 8 shows the observed ROSAT spectrum of ζ Ori together with the spectrum synthesised from the wind structure of Fig. 7. *Both at soft and hard energies, the calculated flux matches the observed flux well*; the maximum deviation, at $\approx$ 0.6 keV, is a factor of 3. The bottom panel of the figure shows the number of photons incident on the detector, both for the time-dependent wind model and for the best fit to the data. From the model spectrum we find $L_x = 5.4 \times 10^{32}$ erg/s, in good agreement with $L_x = 4.9 \times 10^{32}$ erg/s from the data fit. It therefore appears that the line-driven instability is able to generate sufficient amounts of hot gas in the time-dependent wind model to match the ROSAT spectra from these stars.

This comes quite as a surprise for the following reason: the best fit to the ROSAT data of ζ Ori, assuming isothermal hot gas of radius-independent temperature T and volume filling factor f as the thermal X-ray source gives $T \approx 10^{6.5}$ K and $f \approx 0.01$ (Feldmeier et al. 1996), where the filling factor refers to hot gas at the density of the *stationary* wind. While most hot gas in Fig. 7 has indeed temperatures between 10^6 and 10^7 K, the gross density of this gas is (at least) a factor of 30 to 50 below that of the stationary wind, and its filling factor is smaller than 0.5. Since the emission scales $\propto f\rho^2$, this implies that the X-ray flux from the time-dependent structure should be a factor (at least) 20 to 50 below the ROSAT data.

Cooper 1994 from a rather similar wind structure claims instead $\langle L_{\rm cal} \rangle \approx 10 L_{\rm obs}$! However, this result seems to be due to the inadequate assumption that *stationary, radiative* cooling zones should build up behind the strong shocks found in an *isothermal* wind simulation, where the X-ray emission is then calculated from the known properties of such radiative shocks. Especially, since their cooling length scales inversely with the

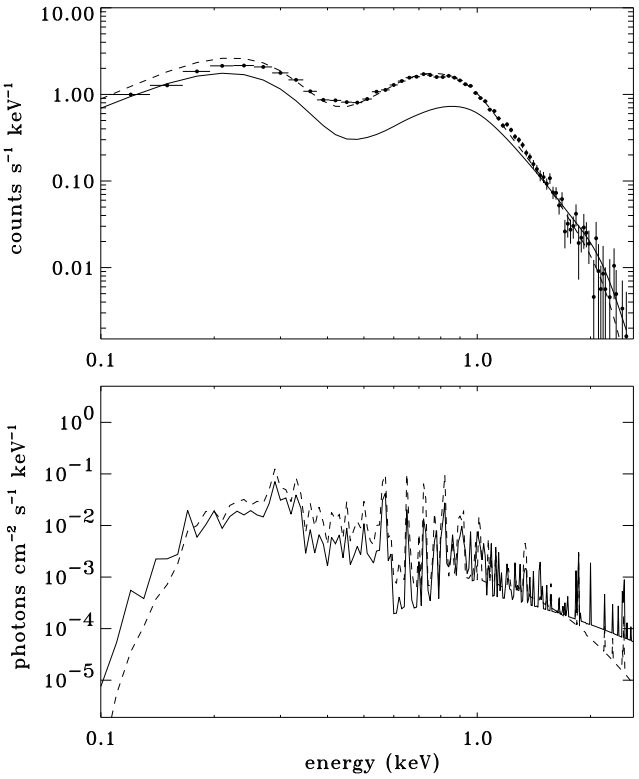

Fig. 8. Upper panel, error bars: ROSAT PSPC spectrum of ζ Ori. Full line: calculated X-ray spectrum from the wind structure of Fig. 7; dashed line: best isothermal fit to the data. Lower panel: number of photons incident on the detector for the wind structure from Fig. 7 (full line) and the best fit to the data (dashed line). The two panels differ by the detector response matrix.

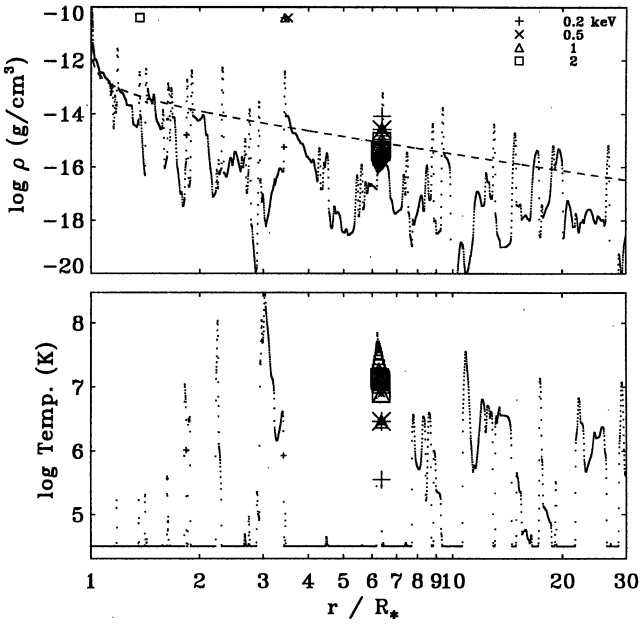

Fig. 9. The wind structure of Fig. 7 again, with the X-ray emitting gas marked: from maximum to minimum size of a symbol (+, x, etc.), the emission $n_{\rm e} n_{\rm H} \Lambda_\nu(T)\,{\rm d}V$ (in erg/s) drops by a factor of 100. The energies corresponding to the different symbols are given at the upper right corner, and the location of wind optical depth unity (where $\tau = 0$ at infinity) at these energies is shown at the upper margin.

preshock density, the low X-ray emissivity ($\sim \rho^2$) of a tenuous gas is partially compensated by the corresponding cooling zone being very extended. However, the rarefied gas in front of reverse shocks from hydrodynamic simulations implies cooling lengths of order (10 to) 100 R_*, i.e., meaningless volume filling factors $\gg 1$ for the typical shock separations of order 1 R_*.

The solution to the above paradoxical situation (i.e., *sufficient* instead of too few X-ray emission from a wind structure with mostly thin, hot gas) comes from Fig. 9, which shows the same snapshot as Fig. 7 but now with the X-ray emission $n_{\rm e} n_{\rm H} \Lambda_\nu(T)\,{\rm d}V$ (units erg/s) from the indicated numerical grid cells of volume ${\rm d}V$. (For our low densities of X-ray emitting gas, the function Λ_ν is practically independent of density). We see that *most X-rays stem from the single shock located slightly above* 6 R_* ("overlooked" in the above estimate) with gas-densities in the hot post-shock region *close to and even exceeding stationary wind densities*. We shall see in the next section that this shock is the site of a shell collision – in which a fast shell is added to the cold, very dense edge of the shock cooling layer – and therefore has rather different properties from the majority of hot gas.

For the moment we notice that only a few shocks (never more than 5; and usually only 1 or 2 dominating ones) emit almost all the observable X-rays in our simulations. This bears some resemblance to the work of MacFarlane & Cassinelli (1989), where a single pair of strong reverse and forward shocks was also found to be able to account for the total X-ray emission from the B0 V star τ Sco.

While the observed and calculated spectra in Fig. 8 agree very well at low energies, there are (at least) two reasons that this coincidence might be fortuitous, and therefore not very significant. (i) In this snapshot, as in most others, the soft component is emitted from a few spatial grid cells only, i.e., the hydrodynamic structure is certainly underresolved for this spectral domain. (ii) The temperature of the gas which emits the soft component is typically in the range from 5×10^5 to 10^6 K – and is therefore certainly affected by our artifical change of the cooling function below $T_{\rm swi} = 4.7 \times 10^5$ K.

We notice that the hard energy tail of the spectrum from the time-dependent simulation in the bottom panel of Fig. 8 shows a shallower decline than the best fit achieved by assuming an isothermal gas at $10^{6.5}$ K. The reason is simply the presence of much hotter gas in the hydrodynamic simulation, and this fact provides an alternative explanation for the possible presence of hard X-ray components in measured spectra instead of the inverse Compton scattering at relativistic electrons (Chen & White 1991), cf. the Introduction.

Fig. 10 shows a greyscale rendition of the contribution function, where the latter gives the *exact* contribution to the total emergent X-ray emission at energy E from gas located within a certain radial range. We find that the emergent spectrum over

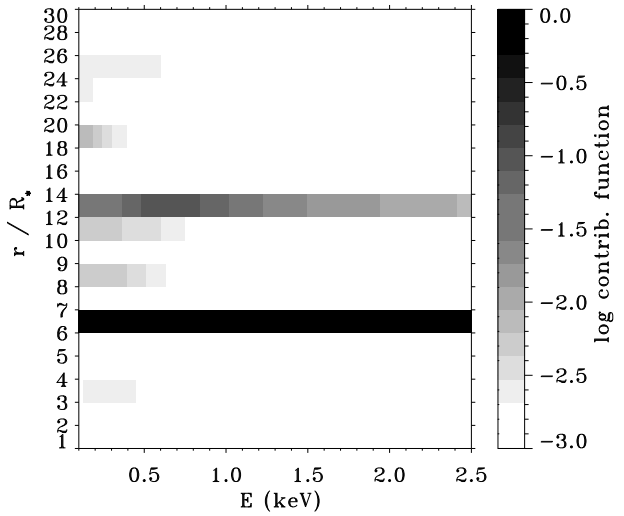

Fig. 10. Greyscale rendition of the contribution function, which is the ratio of emergent X-ray luminosity at energy E (abscissa), from gas located between radii r_i and r_{i+1} (ordinate), to the total emergent luminosity at E.

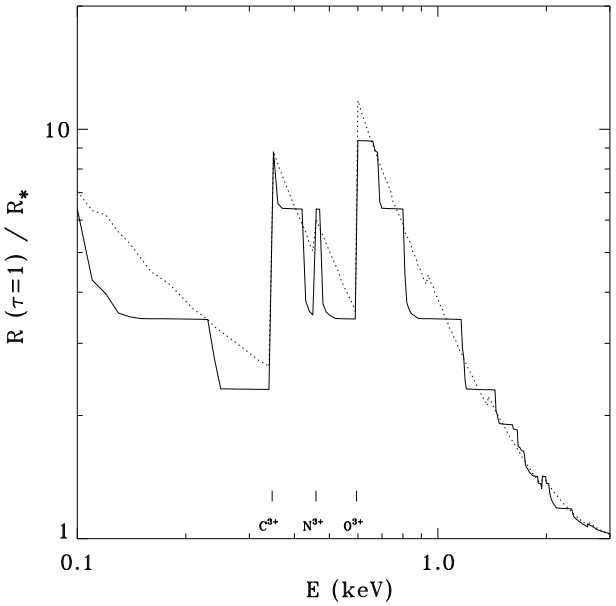

Fig. 11. Location of optical depth unity in the wind, for X-rays in the ROSAT energy range. Full line: time-dependent wind model of Fig. 7. Dashed line: stationary wind model. Three dominant K-shell edges are marked at the bottom margin.

the full ROSAT bandpass is indeed emitted almost single by the shock discussed above. At energies around 0.7 keV, however, a minor contribution of $\approx$ 10% stems from the gas between 12 and 14 R_*. Furthermore, we conclude from this and many other snapshots that more than 90% of the observed X-rays in our models are emitted from below 10 R_*, i.e., from wind regions where acceleration is important.

Fig. 11 shows the location of optical depth unity in the wind (with $\tau = 0$ at infinity) for energies in the ROSAT spectral range. Astonishingly, the $r(\tau = 1)$ curves are rather similar for the time-dependent and the stationary wind model. The reason is that the wind gas can only be compressed once into a shell and then remains there for all subsequent times. Any wind particle can therefore be displaced from its location in the stationary wind by at most the intershell distance, which for radii $r < 10\ R_*$ in Fig. 7 is typically 1 R_* (at most 2 or 3 R_*). The same conclusion holds then for the location of optical depth unity.

Finally, Fig. 12 shows a two-dimensional cut through the emitting and absorbing wind gas. The emitting volumes, as seen by an observer at $r = \infty$, are concentric cylindrical tubes (spherical symmetry is assumed), the terminating surfaces of which (at $\tau \approx 1$) are sections through spheres (at least if the $\tau = 1$ surface lies within a dense shell, which is mostly the case). The reason for the discontinuous jumps of the $\tau = 1$ surfaces at certain values of p is that the optical depth of a shell grows with increasing line of sight angle between z and r, and thus with p.

3.3. Photospheric turbulence as wind perturbation

We repeat in short the discussion from the last section for the model assuming photospheric Langevin turbulence with maximum amplitude $A_{\rm M} = 0.2$ as the triggering perturbation. Fig. 13 shows a snapshot of the wind at 3 d after model start. The most dominant – reverse – shock occurs slightly above 4 R_* here. Shock destruction sets in at $\approx 5\ R_*$ again, and beyond this radius most hot gas is leftover from former shocks only. However, exceptional reverse shocks are also found at very large distances 20 and 27 R_*. Forward shocks with temperatures of order 10^6 K occur at the edges of cold and hot gas at 12 and 15 R_*.

The X-ray emission from the wind structure in Fig. 14 shows again good agreement with the soft and hard regions of the ROSAT spectrum. The maximum deficiency, around 0.7 keV, is by a factor of 4. As before, the hard energy tail of the incident detector spectrum has a shallower decline than the empirical fit using an isothermal emission model with $T_{\rm shock} = 10^{6.5}$ K.

Fig. 15 leads to the same conclusion as was reached in the last section: almost all the emergent X-rays originate from a single, strong reverse shock (of velocity jump 2200 km/s here, and located at $\lesssim 4.5\ R_*$), where the density of the hot, emitting gas is close to and even larger than in a stationary wind. A further contribution at the 10% level (cf. Fig. 16) stems from the outer rim (at $\gtrsim 7\ R_*$) of a broad region of hot intershell gas. As will become clearer in the next section, a shell collision with subsequent shock destruction has just occured at this latter site. Finally, we note that the hot gas seen in the figure below 3 R_* does not contribute significantly to the emergent X-ray radiation, since it is located below the radius where $\tau = 1$ for the corresponding energies.

4. Shell collisions as origin of X-ray emission

To understand the origin of gas heating which leads to X-ray emission, we show in Fig. 17 a greyscale rendition of the wind

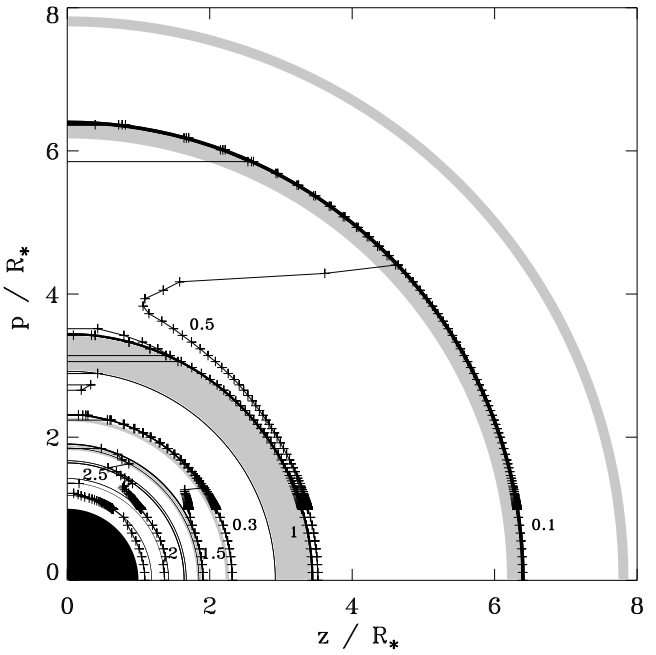

Fig. 12. The (p, z)-geometry of X-ray radiative transfer for the wind structure from Fig. 7. The observer is located at $(z = \infty, p = 0)$. The plus signs, connected by full lines, show the surfaces of optical depth unity at the energies indicated (in keV). The shaded regions show gas hotter than 10^6 K. The narrow, black regions are dense shells where the density is higher than three times the local density of the stationary wind.

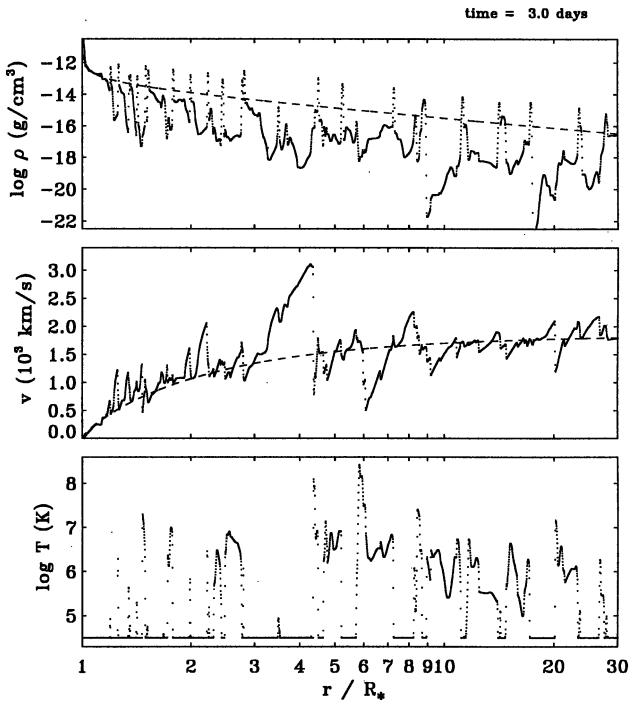

Fig. 13. Snapshot of the wind structure triggered by photospheric Langevin turbulence at three days after model start.

evolution from 3.2 to 4.6 days after model start, with the tunable sound wave as the triggering perturbation. The strong emission at $t = 3.5$ days and $r \gtrsim 6\ R_*$ in Fig. 9 *is now seen to be due to a shell collision*. Even more than that, from the density diagram of Fig. 17 it is clear that significant X-ray emission stems *only* from sites of shell collisions. (The conclusion in the other direction, however, is not true: not every shell collision is the origin of significant X-ray emission.)

We notice from this figure that the snapshot at $t = 3.5$ days appears to be exceptional. While other shell collisions lead to short flashes of X-ray emission (of duration ≈ 500 s; see below), X-rays are generated here over almost 2.5 hours. The reason is that several tiny shells are fed into an outer, pronounced shell, which is then the site of strong emission. Furthermore, we notice that the strongest shell collisions in the figure lead to X-ray flashes still a factor of 10 more intense.

The temperature diagram in Fig. 17 shows a sudden expansion of the cooling zone after each strong shell collision. This is the process of shock destruction (Feldmeier 1995). However, in the latter paper we claimed somewhat misleadingly that the *progressive* rarefication of the intershell gas being fed into the shells causes the broadening of the cooling zones. We now see that the process is instead initiated by an *abrupt* change in preshock conditions after a shell collision: immediately after the merger, extremely rarefied intershell gas is being fed through the shock. This causes radiative cooling to cease and the shock to be pushed into the preshock gas.

The large number of shell collisions in our simulations can be traced back to the existence of two rather different shell populations: (1) very dense shells which move almost according to a stationary wind velocity law. (The fact that most of the gas mass in a time-dependent wind still follows a stationary velocity law was noticed by Owocki et al. 1988, cf. their Fig. 10; see also Puls et al. 1993, Fig. 2); and (2) fast "mini"shells with a density close to stationary values. As is obvious from Fig. 17, in almost all cases the X-ray flash occurs when a fast minishell rams into an outer, pronounced shell. – The formation of pronounced shells can be followed back almost into the photosphere, and corresponds to the largest perturbations which occur there. The momentum the shells gain from faster, inner gas which runs into them (through a reverse shock) is used up again by the shells overtaking and sweeping up dense gas ahead of them (eventually through a forward shock): the shells become fat, not fast. However, with the intershell gas being gradually swept up, ultimately (from about $1.2\ R_*$ on) the remaining gas ahead of the forward shock of a shell can be accelerated (the line-driven instability at work!) all the way through the *broad* and *empty* intershell region, i.e., the momentum is now in a small-mass, high-velocity blob.

Fig. 18 shows a time sequence of the shell collision around $r = 4.2\ R_*$ and $t = 3.64$ d from Fig. 17. We have chosen this instant since it gives a somewhat clearer picture than the multiple collision with very tiny shells at 3.5 days. (We note in passing that two interesting snapshots of a shell collision, however

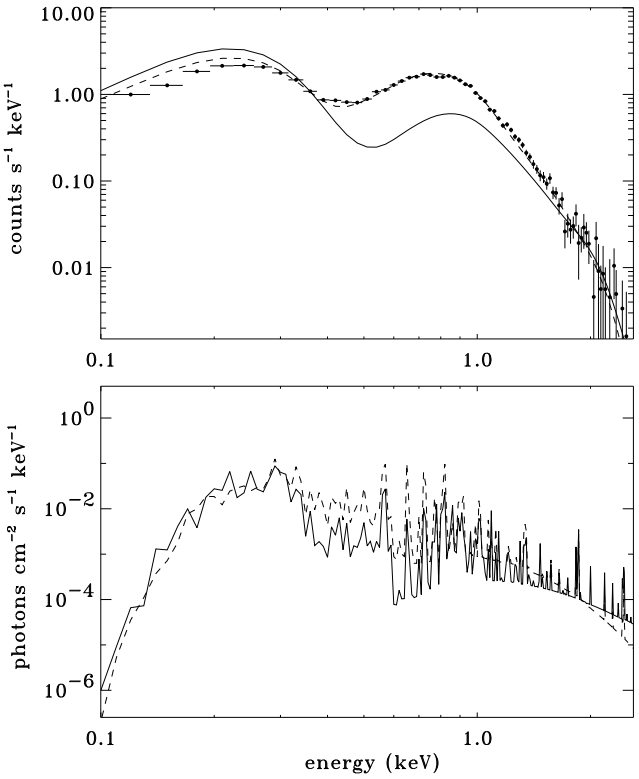

Fig. 14. Upper panel: ROSAT observed spectrum and spectrum for the Langevin model from Fig. 13. Lower panel: number of photons incident on the detector.

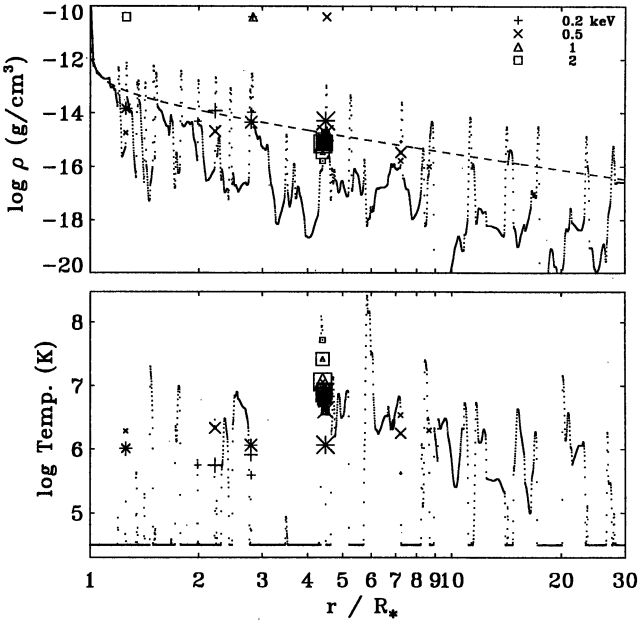

Fig. 15. The Langevin model from Fig. 13, with X-ray emitting gas marked. The symbols are as in Fig. 9.

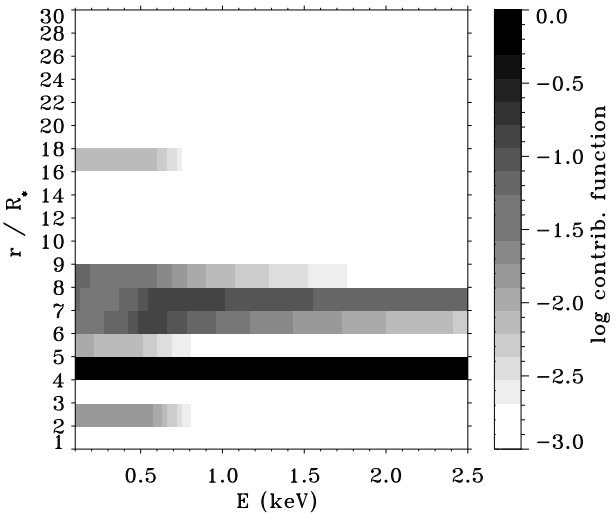

Fig. 16. Contribution function for the Langevin model, cf. Fig. 10.

discussed in the framework of X-ray variability due to shock merging, can be found in Cooper 1994, Fig. 6.9). – The sequence is shown in the frame of a particle which moves through a stationary wind with a $\beta = 0.8$ velocity law, where this particle is initially located at the position of the shell marked *A*. Since the comoving frame coordinate of this shell remains close to 0 during the time series, we see that this shell *is* actually moving roughly according to a $\beta = 0.8$ law. During the first five snapshots of Fig. 18, the fast shell *A'* drives the shock front *B* ahead of it, thereby compressing the cooling zone spanned by *A* and *B*. At 3.62 days, *A'* has merged with *A*. The kinetic energy of relative motion is thermalized during this inelastic collision, and for a short moment both prerequisites necessary for significant X-ray emission are met: the gas has a high density *and* a high temperature. From the figure one finds a relative motion of *A* and *A'* of $\approx$ 700 km/s, which corresponds to a temperature of $\approx 10^7$ K when thermalized. The length scale of this hot and dense region is that of the radiative shock through which the shell *A'* is added to *A*. Due to the high density, radiative cooling is efficient and the cooling zone behind the shock is very thin. Shortly after *A'*, a similar shell *A"* (of relative velocity $\approx$ 800 km/s) merges with *A*, which leads to a stronger X-ray emission at $t = 3.64$ d than the previous merger at $t = 3.62$ d. However, this difference is simply due to the coarse temporal resolution of the sequence. Finally, the last three snapshots of Fig. 18 show that extremely rarefied intershell gas is passing through the shock front; radiative cooling ceases therefore and the shock is pushed into the preshock gas, which ultimately leads to the destruction of the shock.

The duration of such a strong shell collision can be estimated as follows. The thickness of a minishell is the radial extent of swept-up gas – which is a substantial fraction of the intershell distance, i.e., a few times 0.1 R_* – divided by the compression factor, i.e., the Mach number squared at the reverse shock, where Ma = 20 is a typical value in our models. For a relative velocity of 800 km/s between minishell and pronounced shell, the collision time is then of order 10 seconds. Yet, the collision time in our simulations is much longer since we cannot resolve

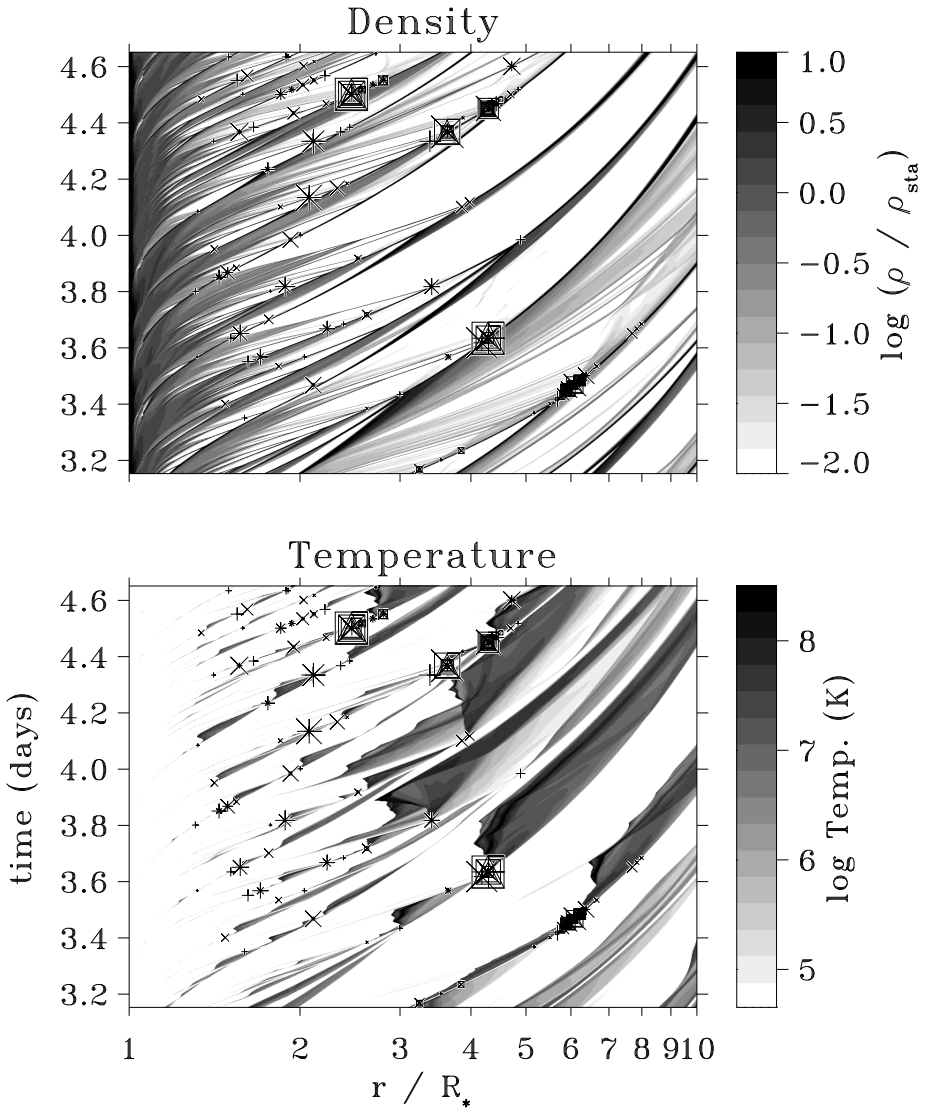

Fig. 17. Greyscale rendition of the evolution of wind density and temperature, with structure formation triggered by a tunable photospheric sound wave. The snapshot of Fig. 7 is taken from this sequence at time 3.5 d. The density is in units of its stationary value, and the coding of the symbols (crosses, squares, etc.) which indicate X-ray emission, $n_e n_H \Lambda_\nu(T)\,dV$, is identical to that in Fig. 9.

the minishells on such tiny length scales, but instead they are smeared out over ≈ 5 grid zones, which gives a collision time of ≈ 500 seconds. However, the amount of heat generated, and therefore of X-rays emitted in the collision depends only on the total mass that is stopped, and should therefore be correctly estimated in our simulations.

We notice that, if the mechanism proposed here is indeed dominant, then the X-ray emission from hot star winds is a true multiscale problem: the total dynamical range of the wind is resolved numerically by $\lesssim 10^4$ grid points; individual wind structures (rarefaction regions between subsequent shells, which possibly collide at later times) by $\lesssim 10^3$ grid points; radiative cooling zones behind strong shocks – which in Feldmeier et al. (1996) were already defined as being of "microscopic" length scale – by $\lesssim 10^2$ points; and the sites of heating during a shell collision – which in the present paper are identified as origin of strong X-ray emission – by $\lesssim 10$ points.

We close this section by considering the energy cascade in the wind from working rate of radiative forces to shock dissipation rate to X-ray emission rate. The first column in Table 2 specifies these numbers for the Lucy & White (1980) blob model, and the second column is an update (White & Chen 1994) for the Lucy (1982) forward shock model. The remaining columns are for the present time-dependent model, i.e., for the snapshots at 3.5 and 3 days of the wind perturbed by sound waves and by Langevin turbulence, respectively.

Here, the individual shocks in the models were examined to find the ratio of wind kinetic energy dissipated in the fronts. The 'efficiency' ratio, η, of heat radiated into X-rays in the ROSAT energy range, $\eta = L_{\rm X,emit}/L_{\rm shock}$, is determined from the constraint that the product of the first four rows in the table gives the ratio $L_{\rm X,emerg}/L_{\rm bol}$ in the fifth row. For temperatures in the range $10^{6.7}$ to 10^8 Kelvin, $\eta > 0.5$ should hold if most of the dissipated energy is radiated away – i.e., if wind heating plays no major role, as is the case in our models.

To gain a clearer view of the energetics of shell collisions, in addition to the snapshots from the last section (column 'total' in the table) we also examined the case when X-ray emission

Table 2. The energy cascade in the wind.

	Lucy & White (1980)	White & Chen (1994)	sound wave		Langevin turb.	
			total	no coll.	total	no coll.
$\frac{L_{\rm wind}}{L_{\rm bol}}$	$3.5 \cdot 10^{-3}$	10^{-2}	$1.7 \cdot 10^{-3}$	...	...	...
$\frac{L_{\rm shock}}{L_{\rm wind}}$	0.1	10^{-2}	$2 \cdot 10^{-2}$	10^{-4}	$2 \cdot 10^{-2}$	10^{-4}
$\frac{L_{\rm X,emit}}{L_{\rm shock}}$	0.1	1	$5 \cdot 10^{-2}$	0.4	$3 \cdot 10^{-2}$	1
$\frac{L_{\rm X,emerg}}{L_{\rm X,emit}}$	$2 \cdot 10^{-3}$	10^{-3}	0.16	0.31	0.15	0.19
$\frac{L_{\rm X,emerg}}{L_{\rm bol}}$	$7 \cdot 10^{-8}$	10^{-7}	$2.8 \cdot 10^{-7}$	$2.3 \cdot 10^{-8}$	$1.7 \cdot 10^{-7}$	$3.3 \cdot 10^{-8}$
$\frac{L^{\rm model}_{\rm X,emerg}}{L^{\rm obs}_{\rm X,emerg}}$	1.3	1	1.1	0.09	0.7	0.13

from collisions is artificially suppressed by setting the gas temperature at these sites to $T_{\rm eff}$ (column 'no coll.' in the table). For the latter case, the steady shocks indeed emit almost all the dissipated energy (which is a fraction 10^{-4} of $L_{\rm wind} = \frac{1}{2}\dot{M}v_\infty^2$) into X-rays, $\eta \lesssim 1$. ($\eta = 0.4$ for the sound wave model indicates that we did not succeed in flagging all collision sites, cf. below.) Yet, the emergent X-ray flux lies a factor of 10 below the observed flux. Including the shell collisions then gives an enhancement of the ratio of wind kinetic energy transformed into heat by a factor of 200. However, the efficiency η drops by a factor of roughly 10, so that now the emitted X-ray flux matches the observed one.

The reason for the reduced efficiency is the following. The dense, narrow shells of gas which pass through some of the fronts at these selected instants are rare events, and lead to a *momentary* dissipation rate (and X-ray emissivity) which is much larger than the true, long-time average. In contrast to a steady shock, the gas conditions in the vicinity of a collision site already imply a much lower dissipation rate and X-ray emission. On the other hand, the X-ray emission as calculated from the snapshot reflects the history of gas heating. The reduction in efficiency reflects then the ratio of the duration of shell collisions (roughly 500 s) to the time interval between them (a few hours).

Our *overall* efficiency of transfering wind kinetic energy into X-rays is more than one decade smaller than in the models of Lucy & White (1980) and Lucy (1982). This is compensated by the lower X-ray absorption in our model. However, this may point to possible difficulties of the present approach to generate sufficient X-ray flux when (much) denser winds are considered.

5. X-ray variability

Since the shell collisions in Fig. 17 occur on a short timescale, and since only a few collisions occur at a given time, the X-ray emission from the wind is highly variable. Fig. 19 shows the X-ray luminosity in the ROSAT band for our four models (two different base amplitudes for each the photospheric sound wave and Langevin turbulence model) together with a fifth model which serves as a numerical test case. The latter has a refined grid in deep wind layers so that filtering of short-scale photospheric waves is reduced. Except for this difference, it is identical to the Langevin model with small base perturbation amplitude. No systematic offset is seen from the figure to occur between these two models, which implies that those photospheric pertubations that are important for the X-ray emission can indeed propagate out into the wind. – Two facts are apparent from the figure (and will be quantified below in Fig. 21):

(1) *The average X-ray luminosity from the models is only a factor of two to three below the observed value.* We feel this to be strong evidence that shell collisions may indeed be efficient enough to generate the X-ray emission from hot star winds. This especially in light of two numerical uncertainties, which both should lead to an *under*estimate of the X-ray flux: first, the resolution problem of radiative cooling zones (cf. Sect. 2.1) leads to a direct loss of hot gas; and second, the cutoff parameter $\kappa_{\rm m}$ (Owocki et al. 1988), which is introduced to make the radiative instability numerically manageable, causes artificial radial stretching of the wind structure, and thereby probably leads to a reduced collision rate along a wind ray.

(2) The $L_x(t)$ distributions of all five models appear to be quite similar. Due to the different perturbation mechanisms applied (sound wave vs. turbulence) this means that our results for the X-ray emission should be robust – even with individual shell collisions being rather delicate processes.

The *minimum* L_x in the figure corresponds to the emission from individual radiative shocks and leftover hot gas, but with no shell-collisions taking place: notice that this minimum lies a factor of ≈ 30 below the observed L_x, as was also estimated in Sect. 3.2 to be the contribution from shocks and old hot gas to the emission. This shows that *shell collisions can lead to an X-ray emission which is on average one order of magnitude larger than the emission from individual shocks and leftover hot gas.*

The question arises whether the L_x at successive instants in Fig. 19 are statistically dependent or independent. The sampling

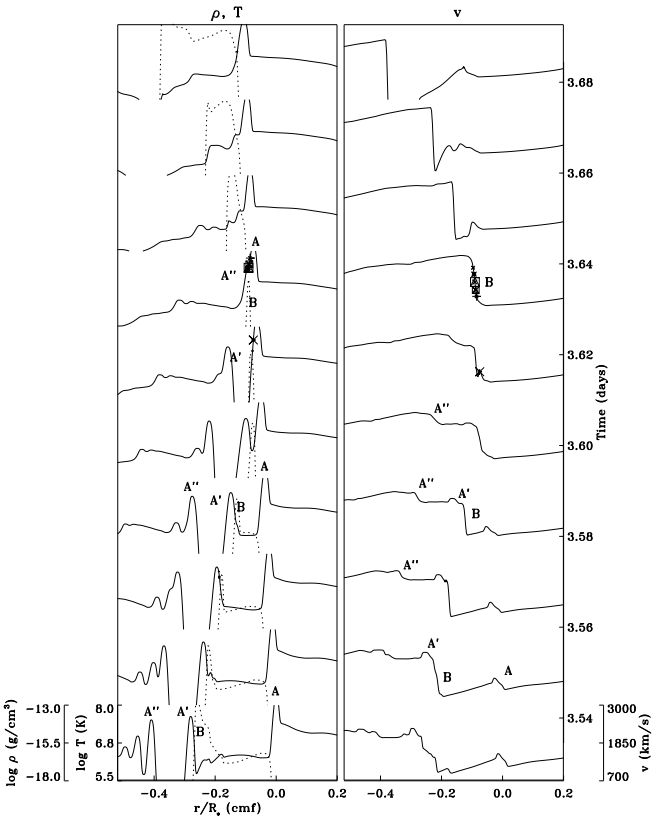

Fig. 18. Time sequence of the shell collision at $r = 4.2\,R_*$ and $t = 3.64$ days from Fig. 17. The left panel shows the density (full line) and temperature (dashed line), the right panel the velocity; axes are indicated for the panel bottom. An outer, pronounced shell, *A*, and two small, inner shells, *A'* and *A"*, are marked. *B* is the reverse shock of shell *A*. The spatial coordinate is in the frame of a particle which moves according to a $\beta = 0.8$ velocity law, and which is initially located at the position of shell *A*.

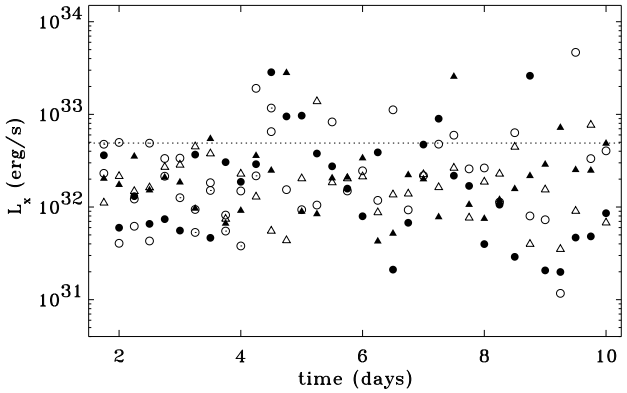

Fig. 19. X-ray luminosity in the ROSAT energy band vs. time, for five numerical wind simulations with different types of base perturbation (triangles: sound wave – circles: Langevin turbulence), and different perturbation amplitudes (open symbols: small – filled symbols: large amplitude). Circles with a dot in the center are for a Langevin test model with very fine grid resolution (this model only up to 4.5 days). The dotted line at $L_x = 4.9 \times 10^{32}$ erg/s is the emergent X-ray luminosity deduced for ζ Ori from a one-temperature fit to the ROSAT data.

time is 6 hours in this plot, i.e., much longer than the interval over which an individual shell collision takes place (about 500 seconds), and also longer than the correlation time of photospheric perturbations, which is between 10^3 and 10^4 seconds. Indeed, at a few instants changes in L_x as large as a factor of 100 are found in Fig. 19 within one sampling time. Therefore, subsequent L_x are – to a large degree – independent. However, there are one, possibly two long-time trends seen in this diagram: (i) up to 4 days, the L_x distribution is narrower than at later times. This is interpreted to be due to the presence of initial transients, i.e., the wind has not yet settled to its limit cycle. (ii) After 4 days, it seems that the width of the L_x distribution grows monotonically with time. However, this is possibly an effect of small sample size in that rare events – i.e., very high or low luminosities – only show up after long time intervals.

One may ask whether it would not be more appropriate to compare time-averaged, synthesised X-ray spectra instead of snapshots with the ROSAT data. While the computational effort in doing so would be high, our results should be rather insensitive to such averaging – at least for the most interesting time intervals of 1000 s, which correspond to typical single ROSAT observations – for essentially two reasons. (1) From a few tests we find that L_x values close to the center of the distributions in Fig. 19 vary only by $\pm 20\%$ over 1000 seconds. (2) The total width of the L_x distributions should also be almost invariant, since: (i) the minimum L_x is due to *frequent* radiative shocks and leftover hot gas; and (ii) the maximum L_x is due to strong shell collisions of duration $\approx$ 500 seconds and $\approx$ 5 hours apart, i.e., this maximum should already be sampled in Fig. 19, and should remain approximately the same under 1000 s averaging.

The temporal average (from 4 to 10 days after model start) of the calculated X-ray spectra is shown in the upper panel of Fig. 20. All four models give, on average, about the correct flux of soft X-rays from 0.1 to 0.4 keV. The largest deviations, by an average factor of ≈ 5, occur for all models between 0.6 and 1 keV. For hard X-rays above 1 keV then, the models predict a flux roughly a factor of 2 or 3 below the observed flux. Furthermore, while the average count rate for the sound wave model with strong base perturbation amplitude (0.5) is, over the whole energy range, almost twice as large as for the small amplitude (0.3) model, the count rate for the turbulence model with small amplitude (0.2) is approximately equal to that with large amplitude (0.5) – actually even somewhat *larger*! Only for the latter Langevin models we can therefore conclude that unstable growth has saturated at a level independent of the base perturbation amplitude before the X-ray emitting region is reached, whereas for the sound wave model the emission (still) scales with the amplitude. The lower panel of the figure shows the ranges spanned by the X-ray spectra during these 6 days. No major systematic offsets between the models are found except for the above mentioned factor of two, and except for an enhanced flux at hard X-rays of the sound wave model with large

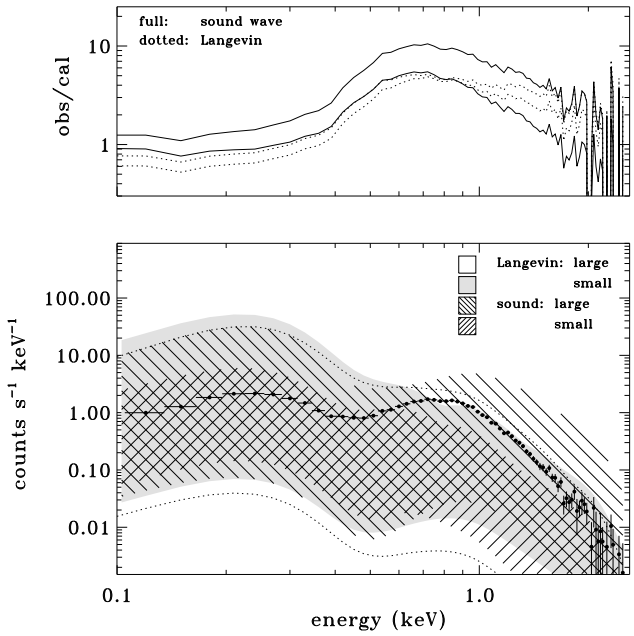

Fig. 20. Temporal variability of the calculated spectra from 4 to 10 days. Upper panel: temporal averages of the observed to calculated count rates. Lower panel: total range of count rates spanned by the different models.

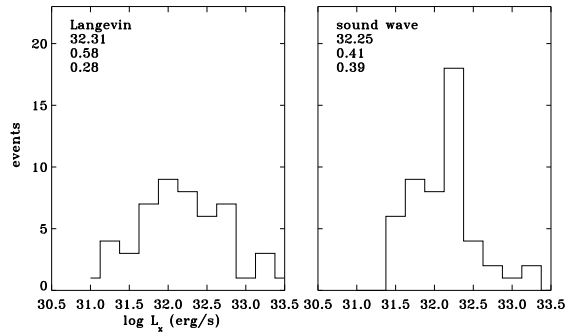

Fig. 21. Distribution function for the Langevin and sound wave model between 4 and 10 days, where "events" refer to Fig. 19. The numbers at top of the panels are the mean value, the standard deviation, and the skewness of the distributions, respectively.

perturbation amplitude. However, the latter hump is spanned up by two snapshots only, i.e., by very sparse events.

We reach the critical test of the present model of X-ray emission. Except for the episodic rise in September 1992, Berghöfer & Schmitt (1994a) found the absolute variations in the X-ray count rate of ζ Ori to be well below 10%. In stark contrast, we find a variability over 2.5 decades in the X-ray luminosity. – We propose, as an outlook to future calculations, that the observed stationarity of the X-ray emission is achieved via a *lateral fragmentation of the emitting and absorbing shells into clouds or clumps*, so that fluctuations along individual wind rays average out over the whole emitting volume. This assumption is consistent with our use of *stochastic* photospheric base perturbations, for which horizontal coherence lengths should be small. (For a typical coherence time t_c = 5000 s in our models, the stellar surface could consist of $\gtrsim 10^5$ patches.) Furthermore, as shown by Rybicki et al. (1990), horizontal velocity fluctuations will be strongly damped due to the line-drag effect (Lucy 1984), hence the line-driven instability should not mix gas from wind rays originating in different photospheric conditions. If, finally, horizontal mixing due to the Rayleigh-Taylor and Kelvin-Helmholtz instabilities (cf. Chandrasekhar 1961) is negligible, and if also the stellar rotation speed is low, we can roughly interpret the temporal snapshots of Fig. 19 as corresponding to the emission from different *radial* cones of small opening angle at one *single* time. To get a quantitative estimate for the required fragmentation then, we argue as follows. We neglect X-ray absorption in the wind (which is not too bad an approximation for ζ Ori); this reduces the radiative "transfer" to a linear problem, one of adding up the emission from individual cones. We assume further that each emitting cone has the same opening angle (i.e., base area), and that the temporal mean and standard deviation of L_x is the same for all cones. From Fig. 21 we find that the mean of the calculated $\log L_x$ distribution is 32.3, with standard deviations $\sigma(\log L_{x,\mathrm{cal}})$ = 0.4 and 0.6 for the sound wave and Langevin models, respectively. Identifying the maximum *absolute* changes of $\leq$ 7% found by Berghöfer & Schmitt (1994a) with a three sigma interval, we have $\sigma(\log L_{x,\mathrm{obs}})$ = 0.01. Since σ drops with the square root of the number of emitting cones, a few thousand independent radial cones would ensure the observed flux constancy.

6. Summary and future work

Our one-dimensional, hydrodynamic model of an O supergiant wind which is subject to the line-driven instability showed that the crash of small, fast blobs into massive, slow blobs can release an X-ray flux which almost matches the observed one. (On the other hand, the X-ray spectral *shape* gives only minor constraints on any model building attempt at this more principal stage – as was also noticed by Cassinelli & Swank 1983, MacFarlane & Cassinelli 1989, and Cooper & Owocki 1994.)

A number of questions were raised during this study, which give the directions for future, more quantitative work.

1. A 3-D Monte Carlo approach is needed for the X-ray transfer which allows patching of the full solid angle into emitting and absorbing wind cones – to study how X-ray flux constancy is achieved via volume averaging. On the other hand a larger number of *radial* shell collisions, and a corresponding reduction in the flux variability could also be achieved by using larger, i.e., more natural values of the cutoff parameter κ_{m} together with shorter perturbation periods. However, methods have to be developed first to handle the steep intershell velocity field that results from increasing κ_{m}.

2. A systematic study is needed over the full range of spectral types O3 to O9 and luminosity classes I to V to find which relation(s) our models predict between L_x and L_{bol} – and other stellar parameters, possibly. The fundamental relation $L_x \approx$

$10^{-7} L_{\rm bol}$ – with no wind quantity entering – remains astonishing for wind-embedded X-ray sources.

3. A detailed investigation of the dynamics of blob-blob collisions is needed, together with a method to achieve better spatial resolution of the blobs and therefore of the collision process in a full hydrodynamic simulation. An interesting question in this context is raised by the finding (Feldmeier et al. 1996) that fits to ROSAT spectra which assume radiative shocks as fundamental emitting entities are superior to fits which assume isothermal hot gas. How does this translate to the present finding that blob-blob collisions are the strongest sites of X-ray emission? Can we identify the radiative shocks from the above fits with the radiative shocks through which small, fast blobs coalesce with pronounced, slow blobs?

Acknowledgements. We thank Drs. S. Owocki, L. Lucy, R.P. Kudritzki, U. Springmann, A. Fullerton, W. Lingl, R. Palsa, and H. Lesch for interesting discussions, and A. Fullerton for carefully reading the manuscript. Most of the ROSAT data for ζ Ori were made available by Drs. J. Schmitt and T. Berghöfer. This work was supported by the DFG under contract Pa 477/1-2, and by the BMBF under contract 50 OR 9304.

References

Abbott D.C., Bieging J.H., Churchwell E., 1984, ApJ 280, 671
Baade D., 1991, in: Baade D. (ed.) Rapid variability of OB stars: nature and diagnostic value. ESO Proc. 36, Garching, p. 217
Baade D., Lucy L.B., 1987, A&A 178, 213
Berghöfer T.W., Schmitt J.H.M.M., 1994a, A&A 290, 435
Berghöfer T.W., Schmitt J.H.M.M., 1994b, Sci 265, 1689
Berghöfer T.W., Schmitt J.H.M.M., 1995, Adv. Space Res. 16, 163
Berghöfer T.W., Baade D., Schmitt J.H.M.M., et al., 1996, A&A 306, 899
Bieging J.H., Abbott D.C., Churchwell E.B., 1989, ApJ 340, 518
Bjorkman J.E., Cassinelli J.P., 1993, ApJ 409, 429
Bohlender D.A., 1994, in: Balona L.A., Henrichs H.F., Le Contel J.M. (eds.) Pulsation, rotation and mass loss in early-type stars. Proc. IAU Symp. 162. Kluwer, Dordrecht, p. 155
Cassinelli J.P., Olson G.L., 1979, ApJ 229, 304
Cassinelli J.P., Swank J.H., 1983, ApJ 271, 681
Cassinelli J.P., Olson G.L., Stalio R., 1978, ApJ 220, 573
Cassinelli J.P., Waldron W.L., Sanders W.T., et al., 1981, ApJ 250, 677
Cassinelli J.P., Cohen D.H., MacFarlane J.J., Sanders W.T., Welsh B.Y., 1994, ApJ 421, 705
Castor J.I., Abbott D.C., Klein R.I., 1975, ApJ 195, 157
Chandrasekhar S., 1961, Hydrodynamic and hydromagnetic stability. Oxford
Chen W., White R.L., 1991, ApJ 366, 512
Chen W., White R.L., 1994, Ap&SS 221, 259
Chlebowski T., Harnden F.R., Sciortino S., 1989, ApJ 341, 427
Cohen D.H., Cooper R.G., MacFarlane J.J., et al., 1996, ApJ 460, 506
Collura A., Sciortino S., Serio S., et al., 1989, ApJ 338, 296
Conti P.S., Ebbets D., 1977, ApJ 213, 438
Cooper R.G., 1994, PhD thesis, Univ. Delaware
Cooper R.G., Owocki S.P., 1992, PASPC 22, 281
Cooper R.G., Owocki S.P., 1994, Ap&SS 221, 427
Corcoran M.F., Swank J.H., Serlemitsos P.J., et al., 1993, ApJ 412, 792
Corcoran M.F., Waldron W.L., MacFarlane J.J., et al., 1994, ApJ 436, L95
Cranmer S.R., Owocki S.P., 1996, ApJ 462, 469
Daltabuit E., Cox D., 1972, ApJ 173, L13
Ebbets D., 1979, ApJ 227, 510
Feldmeier A., 1995, A&A 299, 523
Feldmeier A., Kudritzki R.P., Palsa R., Pauldrach A.W.A., Puls J., 1996, A&A, in press
Fullerton A.W., Gies D.R., Bolton C.T., 1996, ApJS 103, 475
Gail H.P., Hundt E., Kegel W.H., Schmid-Burgk J., Traving G., 1974, A&A 32, 65
Gautschy A., Glatzel W., 1990, MNRAS 245, 597
Gies D.R., 1996, in: Strassmeier K.G., Linsky J.L. (eds.) Stellar surface structure. Proc. IAU Symp. 176. Kluwer, Dordrecht, p. 121
Glatzel W., 1994, MNRAS 271, 66
Harnden F.R., Branduardi G., Elvis M., et al., 1979, ApJ 234, L51
Haser S., 1995, PhD thesis, Univ. München
Hearn A.G., 1972, A&A 19, 417
Hearn A.G., 1973, A&A 23, 97
Hearn A.G., 1975, A&A 40, 277
Henrichs H.F., 1988, in: Conti P.S., Underhill A.B. (eds.) O stars and Wolf-Rayet stars. NASA SP-497, Washington, D.C., p. 199
Henrichs H.F., Kaper L., Nichols J.S., 1994, in: Balona L.A., Henrichs H.F., Le Contel J.M. (eds.) Pulsation, rotation and mass loss in early-type stars. Proc. IAU Symp. 162. Kluwer, Dordrecht, p. 517
Hillier D.J., Kudritzki R.P., Pauldrach A.W., et al., 1993, A&A 276, 117
Kudritzki R.P., 1992, A&A 266, 395
Kudritzki R.P., Hummer D.G., 1990, ARA&A 28, 303
Kudritzki R.P., Lennon D.J., Puls J., 1995, in: Walsh J.R., Danziger I.J. (eds.) Science with the VLT. Springer, Heidelberg, p. 246
Kudritzki R.P., Palsa R., Feldmeier A., Puls J., Pauldrach A.W.A., 1996 in: Zimmermann H.U., Trümper J.E., Yorke H. (eds.) Röntgenstrahlung from the Universe. MPE Report 263, Garching, p. 9
Lamers H.J.G.L.M., Leitherer C., 1993, ApJ 412, 771
Landau L.D., Lifshitz E.M., 1989, Hydrodynamics. Academic Press
Langer S.H., Chanmugam G., Shaviv G., 1981, ApJ 245, L23
Langer S.H., Chanmugam G., Shaviv G., 1982, ApJ 258, 289
Long K.S., White R.L., 1980, ApJ 239, L65
Lucy L.B., 1982, ApJ 255, 286
Lucy L.B., 1984, ApJ 284, 351
Lucy L.B., Solomon P.M., 1970, ApJ 159, 879
Lucy L.B., White R.L., 1980, ApJ 241, 300
MacFarlane J.J., Cassinelli J.P., 1989, ApJ 347, 1090
MacFarlane J.J., Cohen D.H., Wang P., 1994, ApJ 437, 351
MacGregor K.B., Hartmann L., Raymond J.C., 1979, ApJ 231, 514
Mihalas D., 1979, MNRAS 189, 671
Monin A.S., Yaglom A.M., 1987, Statistical fluid mechanics, Vol. 2. MIT Press, Cambridge
Morrison R., McCammon D., 1983, ApJ 270, 119
Norman M.L., Wilson J.R., Barton R.T., 1980, ApJ 239, 968
Owocki S.P., 1991, in: Crivellari L., Hubeny I., Hummer D.G. (eds.) Stellar atmospheres: beyond classical models. Kluwer, Dordrecht, p. 235
Owocki S.P., 1992, in: Heber U., Jeffery S. (eds.) Atmospheres of early-type stars. Springer, Heidelberg, p. 393
Owocki S.P., Puls J., 1996, ApJ 462, 894
Owocki S.P., Rybicki G.B., 1984, ApJ 284, 337
Owocki S.P., Castor J.I., Rybicki G.B., 1988, ApJ 335, 914
Owocki S.P., Cranmer S.R., Fullerton A.W., 1995, ApJ 453, L37
Pallavicini R., Golub L., Rosner R., et al., 1981, ApJ 248, 279
Pauldrach A., Puls J., Kudritzki R.P., 1986, A&A 164, 86

Pauldrach A.W.A., Kudritzki R.P., Puls J., Butler K., Hunsinger J., 1994, A&A 283, 525
Pollock A.M.T., 1987, A&A 171, 135
Pope S.B., 1994, Ann. Rev. Fluid Mech. 26, 23
Prinja R.K., Fullerton A.W., 1994, ApJ 426, 345
Prinja R.K., Howarth I.D., 1986, ApJS 61, 357
Puls J., Owocki S.P., Fullerton A.W., 1993, A&A 279, 457
Puls J., Kudritzki R.P., Herrero A., et al., 1996, A&A 305, 171
Raymond J.C., Smith B.W., 1977, ApJS 35, 419
Raymond J.C., Cox D.P., Smith B.W., 1976, ApJ 204, 290
Reile C., Gehren T., 1991, A&A 242, 142
Risken H., 1989, The Fokker-Planck equation. Springer, Berlin
Rybicki G.B., Owocki S.P., Castor J.I., 1990, ApJ 349, 274
Sciortino S., Vaiana G.S., Harnden F.R., et al., 1990, ApJ 361, 621
Seward F.D., Forman W.R., Giacconi R., et al., 1979, ApJ 234, L55
Stahl O., Wolf B., Gäng T., et al., 1993, A&A 274, L29
Thompson K.W., 1987, J. Comp. Phys. 68, 1
Thompson K.W., 1990, J. Comp. Phys. 89, 439
Uhlenbeck G.E., Ornstein L.S., 1930, Phys. Rev. 36, 823
Underhill A.B., Fahey R.P., 1984, ApJ 280, 712
Van Leer B., 1977, J. Comp. Phys. 23, 276
Voels S.A., Bohannan B., Abbott D.C., Hummer D.G., 1989, ApJ 340, 1073
Walder R., Folini D., 1996, A&A, in press
Waldron W.L., 1984, ApJ 282, 256
Waldron W.L., 1991, ApJ 382, 603
Wax N., 1954, Selected papers on noise and stochastic processes. Dover, New York
Wessolowski U., 1996, in: Zimmermann H.U., Trümper J.E., Yorke H. (eds.) Röntgenstrahlung from the Universe. MPE Report 263, Garching, p. 75
White R.L., 1985, ApJ 289, 698
White R.L., Chen W., 1992, PASPC 22, 274
White R.L., Chen W., 1994, Ap&SS 221, 295

This article was processed by the author using Springer-Verlag LaTeX A&A style file *L-AA* version 3.